LEVEL

AD A099712

Quarterly technical summary rept.
7 Aug - 31 Oct 80.

Solid State Research
1980:4.

1980

This technical report has been reviewed and is approved for publication.

FOR THE COMMANDER

Raymond L. Loiselle, Lt.Col., USAF
Chief, ESD Lincoln Laboratory Project Office

ABSTRACT

This report covers in detail the solid state research work of the Solid State Division at Lincoln Laboratory for the period 1 August through 31 October 1980. The topics covered are Solid State Device Research, Quantum Electronics, Materials Research, Microelectronics, and Analog Device Technology. Funding is primarily provided by the Air Force, with additional support provided by the Army, DARPA, Navy, NASA, and DOE.

CONTENTS

INTRODUCTION

I. SOLID STATE DEVICE RESEARCH

Low-loss GaAs semiconductor optical waveguides have been formed by the lateral epitaxial growth of single-crystal GaAs over SiO_2. Single-mode rib waveguides have exhibited losses of only 2.3 dB/cm, which are 2 to 3 dB/cm lower than those generally reported for GaAs optical waveguides. Furthermore, the guides should have smaller allowable bend radii (<1 mm) than previously reported guides, and could form the basis of a new class of guided-wave structures.

The gain spectra for TE polarization in a GaInAsP/InP laser have been measured as a function of DC bias current below laser threshold. The results have been used to relate the maximum net gain to the nominal current density and radiative quantum efficiency, yielding coefficients important for the optimization of laser design.

High-quality n^+-InP layers over InGaAs have been grown from Sn solutions. The technique is generally applicable to the growth of an alloy of very low As content over one of high As content. The ability to grow these layers may facilitate the fabrication of improved InGaAs lasers and detectors operating at 1.55 μm.

II. QUANTUM ELECTRONICS

A study of the effect of averaging over a large number of pulses indicates that improvement in signal-to-noise ratio in a LIDAR system is limited by statistical variations due to atmospheric turbulence. This has motivated construction of a dual CO_2 differential-absorption system. Initial temporal correlation studies with this system have been made using various targets.

The spectral width of a GaAlAs CW single-mode diode laser has been shown to vary linearly with reciprocal output power at 300 K with a slope 50 times greater than predicted by the Schawlow-Townes expression without the partial inversion factor. Spectral narrowing observed at 77 K for constant mode power is consistent with the predicted temperature dependence of the partial inversion factor.

A program to apply the techniques of nonlinear spectroscopy to diagnostic problems in semiconductors has been initiated. Preliminary results of CARS measurements of phonons and plasmons in a number of semiconductor materials have been obtained.

Liquid N_2 Raman laser characteristics in both tight-focusing and collimated-beam geometries have been investigated. A quantum conversion efficiency of 92 percent into the first Stokes output has been observed for the collimated-beam geometry.

Using molecular beams and a tunable submillimeter laser sideband spectrometer, sub-Doppler linewidth rotational transitions at 700 GHz have been observed for the first time. The separation between two closely spaced CH_3F lines has been measured to an accuracy of 70 kHz.

III. MATERIALS RESEARCH

It has been demonstrated that under suitable experimental conditions the deposition rate of InP layers grown by vapor-phase epitaxy varies significantly with crystallographic orientation, and this orientation dependence has been utilized to obtain structures in which single-crystal InP layers are grown laterally over phosphosilicate-glass films. Structures of this type are of potential interest as waveguides for infrared radiation in integrated optical circuits.

Since amorphous films in the Ge-Si alloy system, as well as films which have undergone amorphous-to-crystalline transitions, have potential applications in solar cells and other devices, differential scanning calorimetry has been used to measure the transition temperature T_t and latent heat of crystallization ΔH for $Ge_{1-x}Si_x$ films covering the entire composition range from Ge to Si. The measured values of T_t and ΔH (per gram) increase linearly with x.

I. Zeroepitaxial Ge films have been grown by solid-phase epitaxy (SPE) on single-crystal $\langle 100 \rangle$ Si substrates and then treated by ion implantation and reannealing to reduce their twin density. Heteroepitaxial GaAs layers of good crystal quality have been grown by chemical vapor deposition on the reannealed Ge films, indicating that it should be possible to use SPE-Ge/Si substrates in the fabrication of low-cost, high-efficiency GaAs thin-film solar cells.

IV. MICROELECTRONICS

The low-light-level characterization of the 100- × 400-element CCD imager being built for the GEODSS (Ground Electro-Optical Deep Space Surveillance) Program has continued. Charge transfer inefficiency of 1.2×10^{-4} per transfer has been measured for charge packets of about 100 electrons, and for larger charge packets a value of less than 1×10^{-5} per transfer has been measured for packets up to 500,000 electrons. Low-light-level operation of the device has revealed a heretofore unobserved trapping mechanism in isolated CCD wells.

Long-term anneals in a hydrogen ambient at temperatures compatible with aluminum metallization ($<500°C$) have proven effective in removing surface states at the SiO_2-Si interface in dual-dielectric (Si_3N_4 over SiO_2) gate structures where the Si_3N_4 acts as a diffusion barrier to the hydrogen. The annealing takes place by lateral diffusion of hydrogen through the SiO_2 under the Si_3N_4, and is initiated at the periphery of the device at openings in the Si_3N_4 layer. Rate measurements of this process made on the GEODSS imager using video techniques are in agreement with published results.

Variations in input-gate capacitance and threshold voltage among the multiple inputs of the previously reported CCD programmable transversal filter structures limit the dynamic range and bit accuracy of these devices. The current CCD fabrication process has reduced the relative input-gate capacitance variation to less than 1 percent on a typical device, and by eliminating the boron offset implant under the surface channel input gates, the threshold voltage variation has been reduced to a 1σ value of 2 mV.

A technique has been developed for integrating Schottky-barrier mixer diodes and FETs in a monolithic GaAs receiver for operation at 31 GHz. For IFs between 2.0 and 2.3 GHz, the conversion gain and noise figure are approximately 4 and 11.5 dB, respectively. Measurement and analysis indicate that with improved matching and two IF amplifier stages a noise figure below 10 dB and a conversion gain of 14 dB can be achieved.

An all-polyimide mask for the proton exposure of resists has been developed, and a resolution of 1.2 μm has been demonstrated with a grating pattern of 1.2-μm lines on 3.8-μm centers. The mask consists of a freestanding polyimide membrane about 2 μm thick with the pattern etched into the membrane to a depth of 1 μm by oxygen reactive-ion etching.

The crystallographic and electrical properties of graphoepitaxial silicon films in which the crystallization was induced with a strip-heater oven have been measured and compared with the properties of graphoepitaxial silicon films in which the crystallization was induced with a scanning laser. The range of orientations of the crystallites in the silicon was considerably reduced for the strip-heater-oven crystallized films. FETs fabricated in oven-crystallized silicon have surface mobilities between 300 and 460 cm^2/V-s, while similar devices could not be fabricated in laser-crystallized films because of surface microcracks.

V. ANALOG DEVICE TECHNOLOGY

A wideband, low-loss, temperature-stable matched filter has been developed using surface-acoustic-wave (SAW) reflective-array-compressor (RAC) technology. This device is fabricated on a special cut of quartz. It has a time-bandwidth (TB) product of 1900, which is comparable with TB products achieved with conventional LiNbO$_3$, but with a temperature stability about 100 times better than LiNbO$_3$ RACs. The quartz RAC incorporates both edge-bonded transducers to achieve 40-percent fractional bandwidth and beam-steering compensation in the etched reflection gratings to achieve 38-μs dispersion.

Controllable attenuation of SAWs on LiNbO$_3$ has been accomplished by using resistive cermet films. Attenuation varying from 0.06 to 0.4 dB/wavelength at 300 MHz was obtained by using sputtered 70% Cr$_2$O$_3$ – 30% Cr films about 1000 Å thick. These rugged and stable films have been used in RAC devices as a contaminant-free method of suppressing edge reflections in order to eliminate spurious responses. Such films appear appropriate to trim the amplitude response of RACs as well.

A hybrid analog/binary signal-processing technique has been developed which offers 40 to 60 dB of processing gain for spread-spectrum communication and wideband radar systems. The hybrid approach is a generic concept which very effectively combines the attributes and compensates for the limitations of the separate techniques alone. Hybrid processing can be implemented with several technologies. A preliminary demonstration employing SAW convolvers with Si integrated circuits has provided the expected 40-dB signal-processing gain.

REPORTS ON SOLID STATE RESEARCH

15 August through 15 November 1980

PUBLISHED REPORTS

Journal Articles

JA No.

5026	Collision Narrowing of HF Fundamental Band Spectral Lines by Neon and Argon	A. S. Pine	J. Mol. Spectrosc. **82**, 435 (1980)
5040	The Effect of Implant Temperature on the Electrical Characteristics of Ion Implanted Indium Phosphide	J. P. Donnelly C. E. Hurwitz	Solid-State Electron. **23**, 943 (1980)
5072	Photo-Acoustic and Photo-Refractive Detection of Small Absorptions in Liquids	S. R. J. Brueck H. Kildal L. J. Belanger	Opt. Commun. **34**, 199 (1980)
5075	Picosecond Optical Sampling	H. A. Haus* S. T. Kirsch* K. Mathyssek* F. J. Leonberger	IEEE J. Quantum Electron. QE-16, 870 (1980)
5096	Atomic Resonance-Line Lasers for Atomic Spectrometry	D. J. Ehrlich R. M. Osgood, Jr. G. C. Turk* J. C. Travis*	Anal. Chem. **52**, 1354 (1980)
5100	Radiometric Observations of the 752.033-GHz Rotational Absorption Line of H_2O from a Laboratory Jet	G. F. Dionne J. F. Fitzgerald T-S. Chang M. M. Litvak* H. R. Fetterman	Intl. J. Infrared and Millimeter Waves **1**, 581 (1980)
5103	Remote Sensing of NO Using a Differential Absorption Lidar	N. Menyuk D. K. Killinger W. E. DeFeo	Appl. Opt. **19**, 3282 (1980)
5109	Crystallization-Front Velocity During Scanned Laser Crystallization of Amorphous Ge Films	R. L. Chapman J. C. C. Fan H. J. Zeiger R. P. Gale	Appl. Phys. Lett. **37**, 292 (1980)
5115	Surface Passivation Techniques for InP and InGaAsP p-n Junction Structures	V. Diadiuk C. A. Armiento S. H. Groves C. E. Hurwitz	IEEE Electron. Devices Lett. EDL-1, 177 (1980)

---

* Author not at Lincoln Laboratory.

[*] Author not at Lincoln Laboratory.

UNPUBLISHED REPORTS

Journal Articles

JA No.

5071	Phase Diagram for LPE Growth of GaInAsP Layers Lattice-Matched to InP Substrates	J. J. Hsieh	Accepted by IEEE J. Quantum Electron.
5120	Avalanche Multiplication and Noise Characteristics of Low Dark-Current GaInAsP/InP Avalanche Photodetectors	V. Diadiuk S. H. Groves C. E. Hurwitz	Accepted by Appl. Phys. Lett.
5124	Paramagnetic-Ion Crystalline Lasers	P. F. Moulton	To be published in Handbook Series on Laser Science and Technology, Volume 1: Lasers in All Media (CRC Press, Boca Raton, Florida)
5127	Heteroepitaxy of $Ge_{1-x}Si_x$ on Si by Transient Heating of Ge-Coated Si Substrates	J. C. C. Fan R. P. Gale F. M. Davis G. H. Foley	Accepted by Appl. Phys. Lett.
5129	A Comparison of Flash-Lamp-Excited $Nd_xLa_{1-x}P_5O_{14}$ (x = 1.0, 0.75, 0.20) Lasers	S. R. Chinn W. K. Zwicker[*]	Accepted by J. Appl. Phys.
5136	Submillimeter Heterodyne Detection of Interstellar CO at 434 μm	H. R. Fetterman G. A. Koepf[*] P. F. Goldsmith[*] B. J. Clifton D. Buhl[*] N. R. Erickson[*] D. D. Peck N. McAvoy[*] P. E. Tannenwald	Accepted by Science
5140	A Balloon-Borne Laser Heterodyne Radiometer for Measurements of Stratospheric Trace Species	R. T. Menzies[*] C. W. Rutledge[*] R. A. Zanteson[*] D. L. Spears	Accepted by Appl. Opt.
5144	Low Dark-Current, High-Gain, GaInAsP/InP Avalanche Photodetectors	V. Diadiuk S. H. Groves C. E. Hurwitz G. W. Iseler	Accepted by IEEE J. Quantum Electron.
5150	Gain Spectra in GaInAsP/InP Proton-Bombarded Stripe-Geometry DH Lasers	J. N. Walpole T. A. Lind J. J. Hsieh J. P. Donnelly	Accepted by IEEE J. Quantum Electron.

---

[*] Author not at Lincoln Laboratory.

---

* Titles of Meeting Speeches are listed for information only. No copies are available for distribution.

* Author not at Lincoln Laboratory.

ORGANIZATION

SOLID STATE DIVISION

A. L. McWhorter, *Head*
I. Melngailis, *Associate Head*
J. F. Goodwin, *Assistant*

R. H. Rediker, *Senior Staff*
P. E. Tannenwald, *Senior Staff*

QUANTUM ELECTRONICS

A. Mooradian, *Leader*
P. L. Kelley, *Associate Leader*

Barch, W. E.	Goodhue, W. D.*
Belanger, L. J.	Hancock, R. C.
Blumberg, W. A. M.	Kildal, H.
Brueck, S. R. J.	Killinger, D. K.
Burke, J. W.	Menyuk, N.
Bushee, J. F.	Moulton, P. F.
Coulombe, M. J.	Osgood, R. M., Jr.
DeFeo, W. E.	Parker, C. D.
Deutsch, T. F.	Peck, D. D.
Ehrlich, D. J.	Pine, A. S.
Feldman, B.	Sullivan, D. J.
Fetterman, H. R.	Williams, G. E.*

ELECTRONIC MATERIALS

A. J. Strauss, *Leader*
J. C. C. Fan, *Assistant Leader*
J. G. Mavroides, *Senior Staff*
H. J. Zeiger, *Senior Staff*

Anderson, C. H., Jr.	Kolesar, D. F.
Button, M. J.	Krohn, L., Jr.
Chapman, R. L.	Mastromattei, E. L.
Davis, F. M.	Nitishin, P. M.
Delaney, E. J.	Owens, E. B.
Fahey, R. E.	Palm, B. J.
Finn, M. C.	Pantano, J. V.
Foley, G. H.	Salerno, J. P.*
Gale, R. P.	Tracy, D. M.
Iseler, G. W.	Tsaur, B-Y.
Kafalas, J. A.	Vohl, P.

APPLIED PHYSICS

R. C. Williamson, *Leader*
C. E. Hurwitz, *Associate Leader*
T. C. Harman, *Senior Staff*
R. H. Kingston, *Senior Staff*

Armiento, C. A.*	Leonberger, F. J.
Calawa, A. R.	Liau, Z. L.
Carter, F. B.	Lind, T. A.
DeMeo, N. L., Jr.	McBride, W. F.
Diadiuk, V.	Paladino, A. E.
Donnelly, J. P.	Plonko, M. C.
Ferrante, G. A.	Spears, D. L.
Foyt, A. G.	Tsang, D. Z.*
Groves, S. H.	Turner, G. W.
Hovey, D. L.	Walpole, J. N.
Kirsch, S. T.*	

ANALOG DEVICE TECHNOLOGY

E. Stern, *Leader*
J. H. Cafarella, *Assistant Leader*
R. W. Ralston, *Assistant Leader*

Anderson, A. C.	Kernan, W. C.
Arsenault, D. R.	Leung, I.
Baker, R. P.	Lowney, S. D.
Becker, R. A.	Lynch, J. T.
Behrmann, G. J.	Oates, D. E.
Brogan, W. T.	Reible, S. A.
Dolat, V. S.	Slattery, R. L.
Fischer, J. H.	Withers, R. S.
Flynn, G. T.	Yao, I.
Holtham, J. H.	

MICROELECTRONICS

W. T. Lindley, *Leader*
F. J. Bachner, *Associate Leader*
R. A. Murphy, *Assistant Leader*
H. I. Smith, *Assistant Leader*

Alley, G. D.	Felton, B. J.	Melngailis, J.†
Bozler, C. O.	Flanders, D. C.	Mountain, R. W.
Burke, B. E.	Geis, M. W.	Nichols, K. B.
Cabral, S. M.	Gaeloe, G. T.*	Placentini, W. J.
Chiang, A. M.	Gray, R. V.	Pichler, H. H.
Chu, A.	Hansell, G. L.*	Rabe, S.
Clifton, B. J.	Hawrylak, A. M.*	Rathman, D. D.
Daniels, P. J.	Lincoln, G. A., Jr.	Shaver, D. C.‡
DeGraff, P. D.	Lyszczarz, T. M.	Silversmith, D. J.
Durant, G. L.	Macropoulos, W.	Smythe, D. L., Jr.
Economou, N. P.	Mahoney, L. J.	Vigilante, J. L.
Efremow, N., Jr.	McClelland, R. W.	Wilde, R. E.
Elta, M. E.	McGonagle, W. H.	

*Research Assistant
†Part Time
‡Staff Associate

I. SOLID STATE DEVICE RESEARCH

A. LOW-LOSS GaAs OPTICAL WAVEGUIDES FORMED BY LATERAL EPITAXIAL GROWTH OVER OXIDE

A number of optical guided-wave devices have been demonstrated in GaAs-based semiconductors.[1] While some of the electrooptical devices have had excellent performance, single-mode three-dimensional guides have had losses of $\geqslant 4$ dB/cm at wavelengths $\leqslant 1.06$ μm, which is appreciably higher than the ~1 dB/cm obtained in many non-semiconductor electrooptic guides. We report here the initial demonstration of a new type of semiconductor optical waveguide with measured attenuation of 2.3 dB/cm at 1.06 μm. Moreover, these guides have the potential for losses as low as 1 dB/cm, should have smaller allowable bend radii than previously reported guides, and could form the basis of a new class of guided-wave structures. The guides are formed by a new lateral epitaxial growth technique[2] in which thin single-crystal GaAs films are grown over SiO_2 layers by vapor-phase epitaxy. These structures will be referred to as oxide-confined waveguides. In this report we will discuss the guide structure and characteristics, briefly describe the epitaxial growth technique, and then present the results of the loss measurements.

One oxide-confined waveguide structure we have fabricated, and for which loss measurements are reported, is a rib guide – shown schematically in Fig. I-1(a). Guiding occurs in the n⁻ epitaxial layer under the etched rib with an SiO_2 film serving as the lower guide boundary and air serving as the upper boundary. By choosing the proper dimensions, single-mode operation can be obtained.[3] There is a stripe opening in the oxide film running parallel to the etched rib, which can be seen in cross section in Fig. I-1(a). This stripe opening is the nucleation region for the epitaxial growth. Other oxide-confined waveguide structures have been fabricated and will be discussed later.

These waveguide structures have a number of potential advantages relative to previously reported semiconductor waveguides. First, the devices have potential for very low loss (~1 dB/cm, or 0.3 cm⁻³). This low attenuation results from residual low loss ($\alpha \sim 0.3$ cm⁻³) in the undoped n-guiding layer,[4] since the vertical confinement by the oxide does not allow the mode tail to penetrate the GaAs substrate (mode penetration depth ~500 Å). In GaAs epitaxial guides it has previously been shown that the loss of ~4 dB/cm is largely due to the tail of the mode in the lossy n⁺ substrates.[5] The high index discontinuity between the GaAs and the air and oxide claddings leads to tight mode confinement. Calculations of the effective index difference Δn for an oxide-confined rib waveguide indicate that values of $\Delta n \gtrsim 10^{-2}$ can be obtained for epitaxial layer thicknesses $\lesssim 2$ μm and rib height of ~0.5 μm. By comparison, $\Delta n \sim 5 \times 10^{-4}$ for GaAs waveguides formed by doping variation, and $\Delta n \sim 5 \times 10^{-3}$ for Ti-diffused $LiNbO_3$ structures. This large confinement should make possible the fabrication of small-radius bends (<1 mm) and, hence, a relatively large packing density for integrated optical circuits. Other structures requiring large index differences, such as waveguide lenses and reflective gratings, should also be feasible. Schottky barriers have been formed on these lateral epitaxial layers and were measured to have the low leakage and sharp high-voltage breakdown typical of devices formed on conventional VPE layers. This suggests that the electrical isolation of the guiding layer from the substrate by the oxide can be utilized to form efficient electrooptic devices having a large spatial overlap of the optical mode and the bias electric field. Design flexibility may be
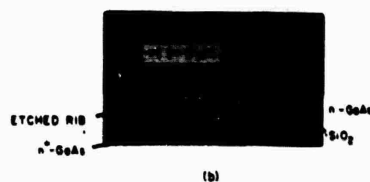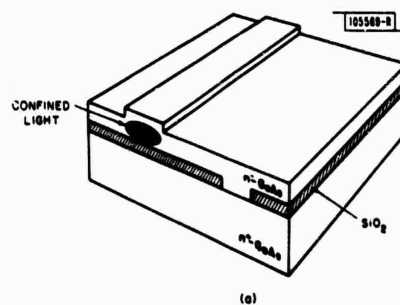
Fig. I-1. (a) Schematic drawing of GaAs oxide-confined rib waveguide.
(b) Photomicrograph of cleaved cross section of guide; 3000-Å-thick
oxide is visible as a thin dark line.
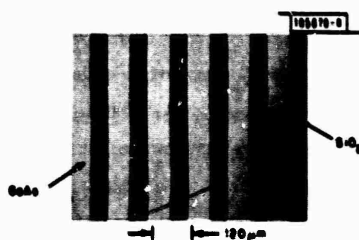
Fig. I-2. Photomicrograph of a portion of surface
of a GaAs wafer used for waveguide fabrication.
Epitaxial growth stripes are 80 μm wide and 4 μm
high, and nucleated from 8-μm openings in the
SiO$_2$ layer.
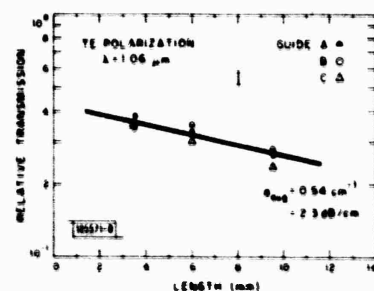
Fig. I-3. Transmission vs length for
single-mode GaAs oxide-confined rib
waveguides. Average TE attenuation
constant for guides at 1.06 μm is
shown by solid line.

further enhanced by the fact that Schottky barriers have also been successfully embedded in epitaxial GaAs.

The GaAs lateral-overgrowth technique has recently been discussed elsewhere[2] and, therefore, is only briefly described here. The crystal-growth process starts with a single crystal of GaAs on which a film of pyrolytic SiO_2 has been formed. Stripe openings are etched in the SiO_2, and the sample is placed in the $AsCl_3$-H_2-Ga vapor-phase growth system. Growth nucleates only in the openings in the SiO_2 film, and for proper choices of crystal orientation, stripe direction, and growth conditions, the single-crystal growth rate parallel to the surface will be much greater than that perpendicular to the surface (lateral-to-vertical growth ratios as high as 25:1 have been achieved). Thus, the growth will proceed rapidly over the oxide surface. If the growth is allowed to continue for a sufficient time, a continuous sheet of GaAs will be formed.

For the waveguides reported here, the growth times and SiO_2 openings were such that the growth stripes did not form into a continuous sheet. Figure I-2 is a photomicrograph of a top view of a portion of a GaAs wafer used to fabricate waveguides. In this case, growth was nucleated from 8-μm openings on 120-μm centers. The pyrolytic SiO_2 was 3000 Å thick and deposited at 400°C. The growth was on [110]-oriented GaAs, and the oxide slot openings were oriented 10° clockwise from the normal to the [$\bar{1}$10] cleavage plane. For the growth conditions used, a 10:1 growth ratio was achieved, resulting in 4-μm-thick epitaxial stripes that were 80 μm wide. The smoothness and uniformity of this single-crystal GaAs surface are evident from the photomicrograph. For this case, the electron concentration was 1×10^{18} cm^{-3} in the substrate and $\sim 1 \times 10^{15}$ cm^{-3} in the undoped epitaxial layer.

A photomicrograph of a cleaved cross section of a finished device is shown in Fig. I-1(b). To form this rib waveguide, 6-μm-wide Ti stripes were patterned on the 4-μm-thick epitaxial layers parallel to and spaced about 10 μm from the oxide-stripe openings. These Ti stripes served as an etch mask, and the GaAs was then chemically etched[5] to the desired depth to form a single-mode waveguide. For this case the etch depth was 0.5 μm. The Ti layer was then chemically removed. It should be noted that in this structure a three-dimensional waveguide is also formed in the oxide-stripe opening. This guide has an inverted rib structure because the effective thickness[3] of the guiding layer in the opening exceeds the epitaxial layer thickness by about 1 μm due to the penetration of the mode tail into the GaAs substrate. Although this oxide-gap guide is also a new waveguide structure, it is of limited interest in the form demonstrated here because of losses resulting from the mode tail in the heavily doped substrate.

The waveguides were tested using an endfire-coupling technique at 1.06 μm with a Nd:YAG laser. A magnified image of the guide near-field output intensity was projected onto both a vidicon camera for display on a television monitor and onto a photodiode for synchronous detection measurements. The devices fabricated were found to support only the fundamental TE and TM modes.

To determine the attenuation coefficient α, loss measurements were made at 1.06 μm on several waveguides on three lengths of the same sample. The guides measured were identical to those described above except that the ribs had a 1-μm etch depth. The measurements were made using a sample-in, sample-out technique on an original guide length of 9.5 mm and then on shorter cleaved lengths of 6 and 3.5 mm. The results for a TE-polarized input are shown in Fig. I-3, where relative guide transmission is plotted vs sample length for three different waveguides. Each data point represents the average of several measurements, and a

representative error bar for the ±10-percent variation in the data is shown. A best estimate for the attenuation constant, obtained by averaging the attenuation constant calculated for each guide, is shown by the solid line. This average α is 0.54 cm^{-1} or 2.3 dB/cm. Similar measurements for TM polarization yielded $\alpha = 0.63$ cm^{-1} or 2.7 dB/cm. These values are the best reported to date for three-dimensional GaAs waveguides at 1.06 μm and are within ~1.5 dB/cm of the previously mentioned theoretical estimate of 1 dB/cm. The additional loss may be due to scattering at the rib edges, since SEM photographs of the etched rib sides showed a roughness of ~500 Å periodicity. Such scattering could be reduced by improving the rib fabrication technique and photolithographic mask quality, or by using a different guide structure.

Other oxide-confined waveguide structures similar to the rib guide of Fig. I-1 have been successfully demonstrated. Single-mode rib guides on semi-insulating Cr-doped substrates have been fabricated, since a high-conductivity substrate is not required as with conventional guides. Planar single-mode inverted-rib guides have also been formed on Cr-doped substrates. For this structure, slots parallel to and spaced 15 μm from the oxide-stripe openings were etched partially through the SiO$_2$ layer. During the epitaxial growth, the slots became filled with GaAs and a planar top surface was formed. Single-mode propagation was observed over the partially etched slots for structures having a 3-μm-thick epitaxial layer and 7-μm-wide, 2000-Å-deep oxide slots.

In summary, oxide-confined GaAs optical rib waveguides have been successfully fabricated with measured attenuation as low as 2.3 dB/cm (0.54 cm^{-1}). This type of waveguide offers a number of advantages over previously demonstrated semiconductor guide structures, including the demonstrated low loss, the electrical isolation from the substrate, and the tight mode confinement and potential for small allowable bend radius. This waveguide structure is made possible by the development of a new lateral epitaxial growth technique in which single-crystal GaAs layers can be formed over SiO$_2$ with lateral-to-vertical growth-rate ratios as high as 25:1. Similar lateral growth may be possible in other semiconductors, such as InP and Si, and the technique could also lead to the development of new active and passive optical guided-wave structures that can be monolithically integrated with other semiconductor devices.

<div align="right">

F. J. Leonberger   I. Melngailis
C. O. Bozler   F. J. O'Donnell
R. C. McClelland

</div>

B. GAIN SPECTRA IN GaInAsP/InP PROTON-BOMBARDED STRIPE-GEOMETRY DH LASERS

We have measured gain spectra for TE polarization in a GaInAsP/InP laser as a function of DC bias current below laser threshold. The measurements were made on a low-threshold device with a stripe geometry defined by proton bombardment. The measurement technique used was the one employed by Hakki and Paoli[6] for similar measurements in GaAs lasers, and is described in detail together with a full discussion of our results in Ref. 7.

Figure I-4 is the spontaneous-emission spectrum for TE polarization taken at a DC bias level of 101 mA for the test device, whose CW threshold current is 117 mA. The spectral resolution is 0.5 Å. If we denote the relative intensity of the emission at one of the maxima of the Fabry-Perot resonances seen in Fig. I-4 by P^+ and the intensity at a neighboring minimum by P^-, then, as shown by Hakki and Paoli,[6] the net gain experienced by the guided light (at a

4
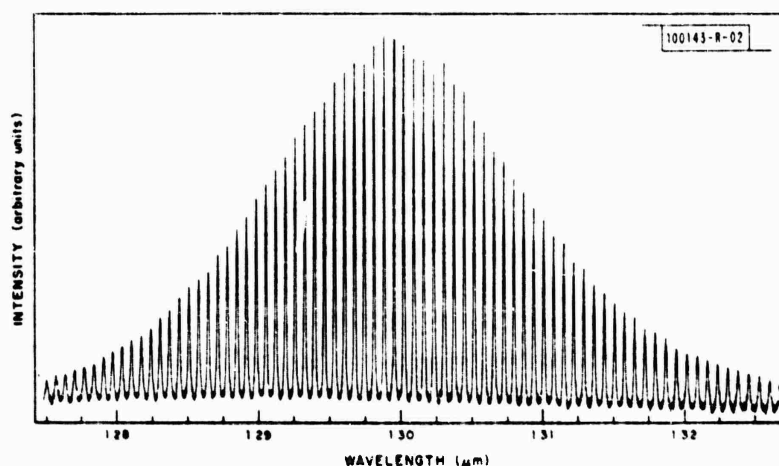
Fig. I-4. Spontaneous-emission spectrum for TE polarization at 101 mA. Structure is due to longitudinal Fabry-Perot modes or resonances of cavity below threshold (117 mA).

wavelength between the wavelengths at the maximum and minimum) is given by

$$-\alpha - \frac{1}{L} \ln \frac{1}{R} = \frac{1}{L} \ln \left[\frac{(P^+/P^-)^{1/2} - 1}{(P^+/P^-)^{1/2} + 1} \right] \tag{I-1}$$

where $-\alpha = \Gamma g - \alpha_i$, in which g is the gain coefficient in the active layer, Γ is the fraction of the optical power density inside the active layer, α_i is the distributed loss coefficient of the mode, L is the cavity length, and R is the mirror reflectivity.

Spectra similar to the one shown in Fig. I-4 were also taken at 60, 70, 80, 90, and 111 mA. We did not analyze data for larger currents (near threshold and above), where the spectral peaks become very narrow and difficult to resolve and the minima approach the background noise level. Also, signals for TM polarization were too low for analysis.

In Fig. I-5 the net gain at each bias current, calculated from the right-hand side of Eq. (I-1), is plotted vs wavelength. The shift of the maximum gain to shorter wavelengths with increased
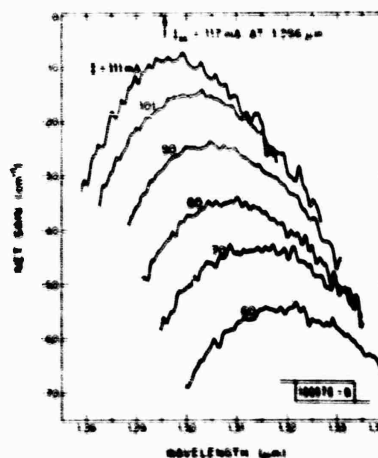
Fig. I-5. Net gain vs wavelength calculated from spontaneous spectrum at each bias current labeled in milliamperes.
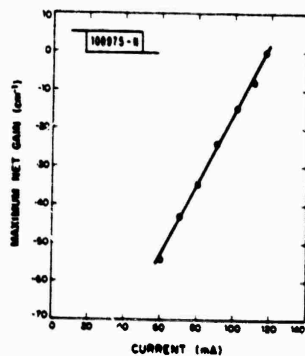
Fig. I-6. Maximum net gain as a function of wavelength plotted vs bias current.

current is expected because of band filling at the higher injection levels. Finally, in Fig. I-6 we have plotted the maximum value of the net gain at each current vs the current. The point at threshold (117 mA) was not obtained from spectral data, but rather was obtained by noting that net gain at threshold is equal to zero by definition. The straight line drawn through the data points fits the equations

$$\Gamma g_{max} - \alpha_i - \frac{1}{L} \ln \frac{1}{R} = -105 + 897I \tag{I-2a}$$

$$= -105 + 0.044J \tag{I-2b}$$

where I is the current in amperes, and J is the current density in A/cm^2.

In order to compare our results with those for GaAs lasers, we need to express g_{max} in the form[8]:

$$g_{max} = \beta(J_{nom} - J_o) \tag{I-3}$$

where β and J_o are parameters to be determined, and the nominal current density J_{nom} is given by $\eta J/d$, with η the quantum efficiency below threshold and d the thickness of the active layer.

Using procedures described in detail in Ref. 7, we estimated from Eq. (I-2b) the following values:

$$\beta \approx 3.1 \times 10^{-2}/\eta \text{ cm } \mu m/A$$

and

$$J_o \approx \eta \times 5.4 \times 10^3 \text{ A/cm}^2 \mu m \quad .$$

These values are comparable to those found for GaAs lasers.[8]

Because our data were obtained from a device with a thin active layer (0.1 μm), our results apply only for large gain (g $\gtrsim$ 150 cm^{-1}) and large J_{nom}.

J. N. Walpole
T. A. Lind
J. P. Donnelly

6

C. n$^+$-InP LPE GROWTH ON InGaAs

The liquid-phase technique of epitaxial growth (LPE) has proved to be well adapted to heterostructure growth of InGaAsP alloys, lattice-matched to InP, for optical-fiber communication applications. One exception to this is the growth of InP over $In_{0.53}Ga_{0.47}As$, or, more generally, the growth of an alloy of very low As content over one of high As content. This problem has become more important as emphasis has shifted from desired operation at 1.3-μm wavelength to that at 1.55 μm. Both lasers and detectors for this longer wavelength have been fabricated; however, adequate growth usually has been achieved at the expense of smaller-than-desired refractive-index and energy-gap discontinuities for lasers and the omission of a contacting window layer for detectors. These factors may have compromised performance. We report here on the growth of high-quality n$^+$-InP layers over InGaAs by use of Sn rather than In solutions. This technique is directly applicable to the growth of avalanche-photodiode structures.[9]

When overgrowth on InGaAs by InP from In solution is attempted, there is a rapid dissolution of the InGaAs which leads to a rough interface and poor morphology of the InP layer. (Recently, this dissolution has been attributed to rapid diffusion of As in the solution.[10]) In order to achieve good epitaxial overgrowth, it is necessary to decrease the rate of the InGaAs dissolution and/or increase the rate of deposition of InP (see Ref. 11). The former can be accomplished by lowering the growth temperature, but this reduces the solubility of InP in the In and, thus, decreases the rate of deposition. (More accurately, the reduced solubility is accompanied by a reduced temperature dependence of the solubility, which determines the rate of deposition.) Increasing the supercooling helps, but not enough to give satisfactory overgrowth from In solutions.

A comparison of the InP solubility data for various solutions[12,13] suggests that the dissolution/deposition situation should be considerably improved for Sn solutions. Figure I-7

Fig. I-7. InP solubility in Sn and In solutions. Solid line for Sn solutions is from experimental data of Ref. 13. Circles are from present experiment; because of pressure loss in our open-tube LPE system, they lie below closed-tube results of Ref. 13. For In solutions, solid line is average of data from Refs. 13 and 14.
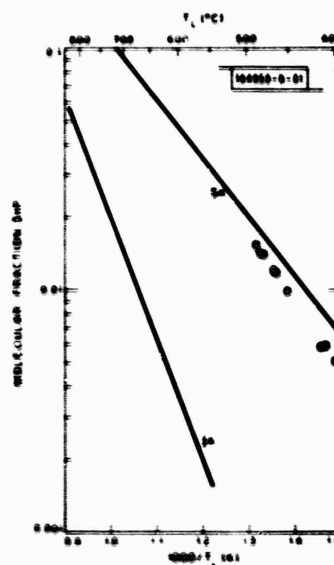
shows curves from Refs. 13 and 14 together with our measurements for InP-Sn solutions. The rate of deposition of InP from Sn solution at 450°C, for example, is comparable to that from In solution at 700°C, and at temperatures as low as 450°C the rate of InGaAs dissolution should be much reduced.
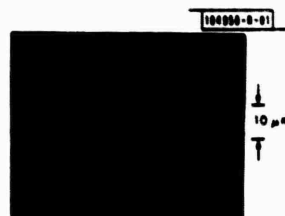
Fig. I-8. Cross section of n^+-InP/InGaAs/InP growth showing high-quality interfaces for both layers of epitaxial growth.

Figure I-8 is a photomicrograph of the cross section of a n^+-InP/InGaAs/InP structure grown using the Sn solution. The high quality of both growth interfaces is apparent. Because of the relatively high phosphorous pressure over the Sn solution (a property that has recently been exploited for prevention of substrate thermal decomposition[14]), this growth was made in two steps. First, the InGaAs was grown on an InP substrate at 645°C. Then, after the growth apparatus was cooled to room temperature and the components of the InP-Sn solution were added, then n^+-InP was grown at 470°C. Presumably, a capped InP-Sn solution would prevent phosphorous contamination of the InGaAs growth solution, and the double-layer growth could be made without a separate addition of the components for the n^+-InP solution. From electrical measurements made on similar n^+-InP layers grown on semi-insulating InP(Fe) substrates, the donor concentration is found to be 3.5×10^{19} cm^{-3} and the room-temperature electron mobility to be 450 cm^2/V·s. Within the source-broadening limitations of the single-crystal x-ray-diffraction technique, the x-ray lines of the InP(Sn) are the same as those of bulk InP.

Finally, it is noted that this technique is useful for n^+-InP/n-InGaAs/n-InP/p^+-InP inverted-mesa avalanche photodiodes, where a thin window layer of n^+-InP over the n- or n^--InGaAs is used to prevent carrier depletion to the surface. For laser structures a p-type InP overgrowth of the InGaAs (or the InGaAsP alloy with emission at 1.55 μm) is desired. Growth from Cd solution might prevent the InGaAs dissolution, but the resulting p^+-InP layer, aside from possible problems with the formation of Cd_3P_2, would have excessive free-carrier absorption loss for the laser structure. Other solutions doped with small amounts of Zn might produce suitable layers. The reader is referred to the precautionary note by Buehler and Bachmann on the high phosphorous pressures that are present over Pb and Bi solutions.[13]

S. H. Groves
M. C. Plonko

REFERENCES

1. For a recent review, see D. Botez and G. J. Herskowitz, Proc. IEEE **68**, 689 (1980).

2. R. W. McClelland, C. O. Bozler, and J. C. C. Fan, Appl. Phys. Lett. **37**, 560 (1980); also Solid State Research Report, Lincoln Laboratory, M.I.T. (1980:2), p. 19, DTIC AD-A092724.

3. E. A. J. Marcatili, Bell Syst. Tech. J. **53**, 645 (1974).

4. G. E. Stillman, C. M. Wolfe, J. A. Rossi, and H. Heckscher, Appl. Phys. Lett. **28**, 197 (1976), DDC AD-A027008/2.

5. F. J. Leonberger, J. P. Donnelly, and C. O. Bozler, Appl. Phys. Lett. **28**, 616 (1976), DDC AD-A027103/1.

6. B. W. Hakki and T. L. Paoli, J. Appl. Phys. **46**, 1299 (1975).

7. J. N. Walpole, T. A. Lind, J. J. Hsieh, and J. P. Donnelly, "Gain Spectra in GaInAsP/InP Proton-Bombarded Stripe-Geometry DH Lasers," to be published in the IEEE Journal of Quantum Electronics.

8. H. C. Casey, Jr. and M. B. Panish, Heterostructure Lasers, Part B (Academic Press, New York, 1978), pp. 180-187.

9. V. Diadiuk, S. H. Groves, and C. E. Hurwitz, Appl. Phys. Lett. **37**, 807 (1980).

10. L. W. Cook, M. Feng, M. M. Tashima, R. J. Blattner, and G. E. Stillman, Appl. Phys. Lett. **37**, 173 (1980).

11. M. Quillec and J. L. Benchimol, Proc. 1980 NATO-sponsored InP Workshop, Harwichport, Massachusetts, 17-19 June 1980, p. 207.

12. A. Leonhardt and G. Kühn, J. Less-Common Metals **37**, 310 (1974).

13. E. Buehler and K. J. Bachmann, J. Cryst. Growth **35**, 60 (1976).

14. J. J. Hsieh, "Thickness of InP Layers Grown by LPE from Supercooled Solutions," Chapter 2 in Gallium Arsenide and Related Compounds (St. Louis) 1976 (The Institute of Physics, London, 1977), pp. 74-80. DDC AD-A046988/2.

15. G. A. Antypas, Appl. Phys. Lett. **37**, 64 (1980).

II. QUANTUM ELECTRONICS

A. TEMPORAL STATISTICS OF LIDAR RETURNS

The differential-absorption LIDAR system has been modified to include a high-speed digital-data-acquisition system capable of collecting and performing statistical analyses of LIDAR returns normalized on a pulse-to-pulse basis to the transmitted laser energy.[1,2] This system was used to study the signal-to-noise enhancement achievable by averaging over increasing numbers of LIDAR returns. The measurements consisted of averaging over a set of N normalized LIDAR returns from an extended diffuse target (side of building) at a range of 2.6 km. Several values of N between N = 1 and N = 5000 were investigated, and ten distinct sets of measurements were taken for each value of N used. The standard deviation of the mean was then determined for the ten sets corresponding to each value of N. Similar measurements were simultaneously made for the normalized signal obtained from a portion of the laser beam after passage through a laboratory absorption cell.

The results of both measurements are given in Fig. II-1. For N < 100 pulses, the signal through the cell is seen to yield a slope of approximately $-1/2$, which corresponds to the predicted $\sqrt{N}$ improvement. For N > 100, the standard deviation approaches a constant value of
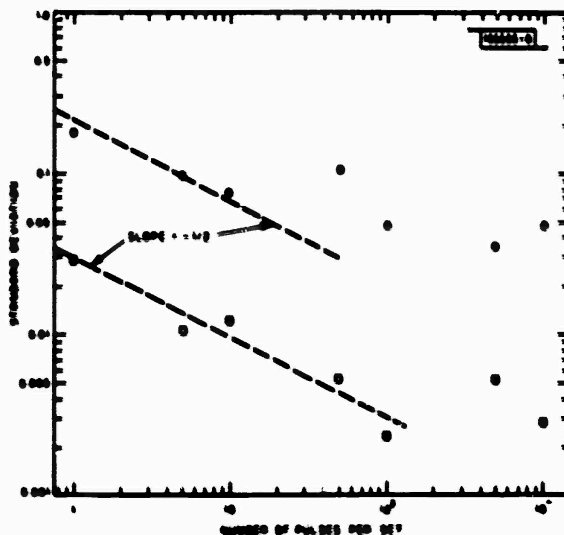
Fig. II-1. Standard deviation of mean of ten sets of normalized LIDAR return pulses as function of number of pulses per set. Returns were obtained from extended diffuse target at range of 2.6 km (circles refer to LIDAR returns, squares to signals obtained after passage through absorption cell).
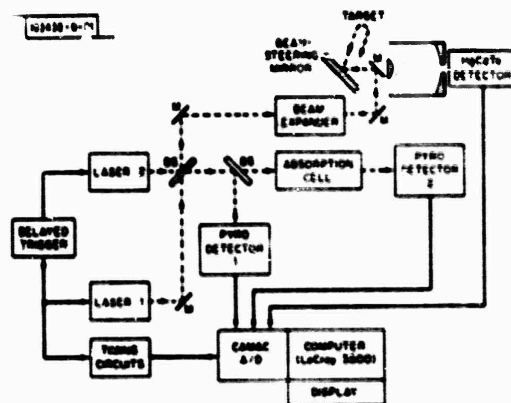
Fig. II-2. Dual CO_2 differential-absorption system.
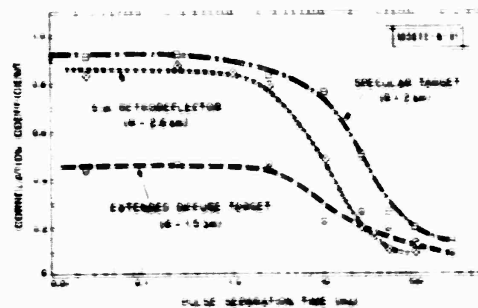
Fig. II-3. Correlation coefficient as function of pulse separation time of CO_2 lasers for retroreflector, specular, and extended diffuse targets.

12

about 0.003; this value is approximately the digital quantization error of the data-acquisition A/D system. For the case of the normalized LIDAR return, the standard deviation for small N is seen to decrease with increasing N at a slower rate than the predicted slope of $-1/2$, and then appears to saturate at a standard deviation of approximately 3 to 4 percent. Similar results obtained with other targets seem to indicate that atmospheric turbulence and target effects set the limit to the enhancement achievable by increasing the number of LIDAR pulses averaged. Furthermore, the data indicate that this limit is reached for integration times on the order of a few seconds.

As a possible means of overcoming such temporal effects, the system was further modified by changing it from a single- to a dual-laser differential-absorption LIDAR system as shown in Fig. II-2. Two line-tunable mini-TEA CO_2 lasers[3] provide the coherent radiation; the pulse delay between the lasers can be varied from about 3 μs to greater than 200 ms.

Our initial measurements with this system involved a study of the temporal correlation of the dual-laser LIDAR returns, where the temporal crosscorrelation coefficient $\rho(x,y)$ is defined by

$$\rho(x,y) = \frac{<(x_i - \bar{x})(y_i - \bar{y})>}{[<(x_i - \bar{x})^2><(y_i - \bar{y})^2>]^{1/2}} = \frac{<(x_i - \bar{x})(y_i - \bar{y})>}{\sigma_x \sigma_y} \qquad (II-1)$$

where x_i and y_i are the normalized LIDAR returns of the ith pulse of the leading and delayed lasers, respectively, and σ_x, σ_y are the standard deviations of the normalized LIDAR returns from the respective lasers. The angle brackets correspond to ensemble averages. Computation of the temporal correlation of the LIDAR pulse pairs, based on Eq.(II-1), was carried out by the data-acquisition system in real time with both lasers operating on the P(24) line (10.632 μm) at a PRF of 15 Hz.

The measured temporal crosscorrelation coefficients of the normalized LIDAR return as a function of the pulse separation time are given in Fig. II-3. The values shown were obtained from a retroreflector at a range of 2.6 km a specular target consisting of metal light fixtures atop a pole 2 km distant, and from the side of a building 1.5 km away which served as an extended diffuse target. The correlation coefficients measured are seen to be essentially constant for delay times up to about 1 to 3 ms, then decrease with further increases in the delay time. Our results are in general accord with recent measurements by Marthinsson et al.[4], which were made using chopped CW CO_2 lasers and a retroreflector.

As expected, the specular target and retroreflector yield high pulse-pair correlation at short pulse delay times. However, the correlation measured for the diffuse target is seen to be limited to a value of approximately 0.5. This limitation was also found to apply to several other diffuse targets investigated. The observed difference may be due to the different statistics of LIDAR returns from specular and diffuse targets. This difference is illustrated in Fig. II-4, which shows histograms obtained from 2000 successive pulses of the normalized LIDAR returns from each of the three targets discussed. The retroreflector and specular-target returns display a nearly log-normal distribution, with large deviations from the mean; by contrast, the distribution of the diffuse target returns is only slightly skewed from a normal distribution with a standard deviation which is smaller by a factor of approximately 3 relative to that of the specular target. These results are consistent with the expectation that returns from small specular targets will be more sensitive to turbulence-caused beam wander or angle-of-arrival effects than
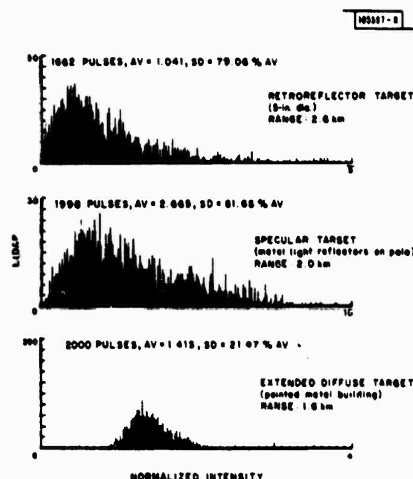
Fig. II-4. Histograms of 2000 normalized LIDAR
returns from retroreflector, specular, and ex-
tended diffuse targets.

will a diffuse target with an essentially angle-independent reflectivity. The smaller deviation
from the mean, coupled with decorrelation effects associated with speckle, may account for the
poor correlation observed from diffuse targets even at the shortest pulse separation times
investigated.

The results obtained with a single-laser system, as given in Fig. II-1, indicate that the im-
provements attainable by averaging over a large number of pulses may well be limited by statis-
tical variations due to atmospheric turbulence long before theoretical detector noise limitations
are approached. We plan to conduct similar experiments with the dual-laser system to establish
if pulse averaging techniques can be made more effective. In addition, our temporal correlation
results appear to show that a dual-laser system can, at best, be only partially effective in freez-
ing out turbulence effects on LIDAR returns from topographic targets.

N. Menyuk
D. K. Killinger

B. FUNDAMENTAL LINE BROADENING OF SINGLE-MODE GaAlAs DIODE LASERS

Although emission linewidths have been reported previously for various semiconductor
lasers operating under diverse conditions,[5-8] heretofore no systematic determination of the
dependence of linewidth on mode power has been made. The importance of a thorough under-
standing of linewidth broadening in single-mode diode lasers is increasing as those devices are
considered for practical applications in frequency-modulated data links, interferometric trans-
ducers, laser gyros, and high-resolution spectroscopy. In the experiment described here, the

14

linewidth of a single-mode Hitachi HLP-1700 laser diode was measured as a function of injection level, with the result that the width decreases linearly with reciprocal mode power but at a rate approximately 50 times greater than that predicted by the Schawlow-Townes formula without the partial inversion factor.[9]

The laser had a threshold of 68 mA and an emission spectrum which became essentially single-mode for injection currents above 80 mA. For currents above 88 mA, the total intensity of the neighboring longitudinal modes was less than 1 percent of the lasing mode intensity. The device oscillated at a wavelength of 817.5 nm at 295 K. The diode was 280 μm long, with a 7-μm stripe width and a 0.1-μm active-region thickness. The material absorption coefficient α was determined to be 45 cm^{-1} from a measurement of the external differential efficiency. Laser temperature was stabilized by mounting the diode package on a copper heat sink in a vacuum. The temperature was sufficiently stable so that the laser drift was much less than 1 MHz/s.

The diode laser linewidth was analyzed by a scanning Fabry-Perot confocal interferometer with a resolution of 3.5 MHz. Besides the measurements taken with the Fabry-Perot interferometer, the linewidth of the single-mode diode laser was observed by heterodyning the output with a highly stabilized, narrow-linewidth external cavity GaAlAs diode laser operating in the same wavelength range.[10] The external-cavity diode laser had a short-term (1 s) rms frequency jitter of 500 kHz. Analysis of the heterodyne spectra indicated that the spectral lineshape of the Hitachi laser was Lorentzian.

Fig. II-5. Linewidth of single-mode output of Hitachi HLP-1700 diode laser at room temperature as function of reciprocal output power. Error is ±1.5 MHz for output power greater than 5 mW, and ±5 MHz for two points at lower power. Solid line is least-squares fit to data.
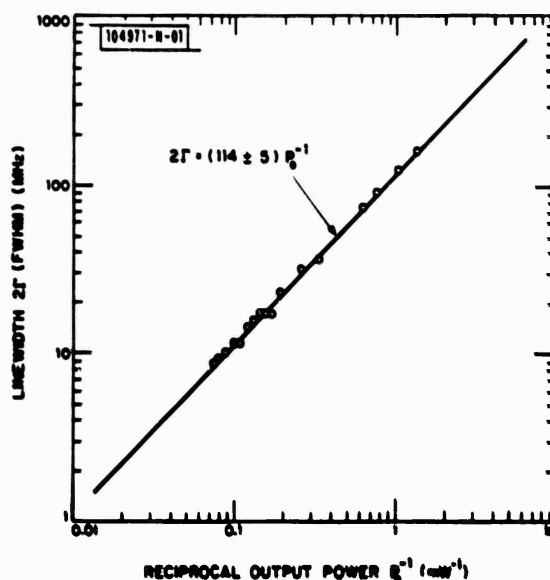
Results of the determination of linewidth vs reciprocal power are illustrated in Fig. II-5. The data, corrected for instrumental resolution, were fitted to a straight line described by 2Γ (MHz) = (114 ± 5) P_o^{-1} (mW^{-1}). The predicted linewidth due to quantum phase fluctuations is given by the modified Schawlow-Townes relation[9]

$$2\Gamma = (h\nu/8\pi P_o)\,(c/n\ell)^2\,(\ell nR - \alpha\ell)\,(\ell nR)\,n_{sp} \qquad (II-2)$$

15

where 2Γ is the full width at half-maximum of the emission line at frequency ν, P_o is the single-ended output power, n is the refractive index, l is the cavity length, α is the material absorption coefficient, R is the facet reflectivity, and n_{sp} – the spontaneous emission factor – is the ratio of the spontaneous emission rate per mode to the stimulated emission rate per laser photon. In a semiconductor laser, n_{sp} may be written as[11]

$$n_{sp} = \left\{ 1 - \exp\left[(h\nu + E_{Fv} - E_{Fc})/kT \right] \right\}^{-1} \qquad (II\text{-}3)$$

where E_{Fc} and E_{Fv} are the conduction- and valence-band quasi-Fermi levels, k is the Boltzmann constant, and T is the temperature. In most lasers, n_{sp} is nearly unity; but for semiconductor lasers with nondegenerate carrier distribution functions, n_{sp} can become significantly greater than unity. The striking feature of Fig. II-5 is the expected linear dependence of the linewidth on reciprocal power, but with a slope fifty times greater than calculated from Eq. (II-2) for $n_{sp} = 1$. Parameter values for the GaAlAs laser used here are known accurately enough to provide a cavity linewidth determination of better than ±20 percent. The biggest uncertainty in the factor n_{sp} is the difference $(E_{Fc} - E_{Fv}) - h\nu$. A value of nearly 0.5 meV for $(E_{Fc} - E_{Fv}) - h\nu$ could account for the observed factor of 50. This parameter is difficult to determine independently, but a value of 0.5 meV would seem too small at room temperature.

Measurements were carried out at liquid nitrogen temperature in order to determine if the linewidth narrowed as predicted by Eq. (II-3). For single-mode output powers up to 3 mW, the observed slope was approximately three times smaller than that observed at room temperature, where the measurements were made in the range 3 to 15 mW. This observation is entirely consistent with Eq. (II-3). It is interesting to note that the ratio $(n_{sp})300$ K$/(n_{sp})77$ K is only weakly dependent upon the parameter $(E_{Fc} - E_{Fv}) - h\nu$, ranging from 3.9 to 2.0 as $(E_{Fc} - E_{Fv}) - h\nu$ goes from 0 to 15 meV. Values of the parameter $(E_{Fc} - E_{Fv}) - h\nu$ greater than 15 meV would be unlikely for the range of conditions in the present experiment, and less than 0 would not satisfy the laser threshold condition. For power levels above 3 mW at liquid nitrogen temperatures and all power levels at liquid helium temperature, the diode output became multimode causing appreciable broadening to the width of each frequency due to mode competition. Changes in the cavity parameters with temperature were estimated to be small enough not to significantly alter the linewidth.

Equation (II-2), describing the phase-fluctuation contribution to the laser frequency, emerges from the assumption that the laser gain is not strongly saturated. This case was treated for semiconductor lasers by Haug and Haken.[11] Elesin and Rusakov[12] later showed theoretically that, in the strongly saturated regime, the Schawlow-Townes formula must be multiplied by a power-independent factor of the order of 100 to 1000. This theory may contribute to the linewidth, but experiments should be carried out at liquid helium temperature on a single-mode device in order to reduce n_{sp} to unity and thus determine any residual contributions to the linewidth.

<div align="right">

M. W. Fleming
A. Mooradian

</div>

C. NONLINEAR SPECTROSCOPY OF SEMICONDUCTORS

An investigation of the potential of nonlinear spectroscopic techniques as semiconductor material diagnostic tools has been initiated. These methods will be applied to spatially resolved deep- and shallow-level impurity and free-carrier measurements as well as to the study of

lattice properties. Techniques to be investigated include coherent anti-Stokes Raman scattering (CARS), Raman gain, and Raman-induced Kerr effect (RIKE). In all these techniques two laser beams at frequencies ω_1 and ω_2 are incident on the semiconductor, and the frequency difference between the two lasers ($\omega_1 - \omega_2$) is tuned to a two-photon or Raman transition. The differences between the techniques are in the detection schemes. In CARS, two pulsed lasers are used, and a mixing signal at the four-wave mixing frequency $2\omega_1 - \omega_2$ is detected. Both of the other techniques use a pulsed laser pump and a CW probe and detect amplitude and polarization effects, respectively, on the probe laser propagation in the sample due to the presence of the pump laser beam.

We have carried out initial CARS measurements of the phonon bands of GaAs, Si, and InP. In addition, coupled plasmon-phonon modes have been observed in n-type GaAs. The experimental arrangement is shown schematically in Fig. II-6. The fixed-frequency laser source is
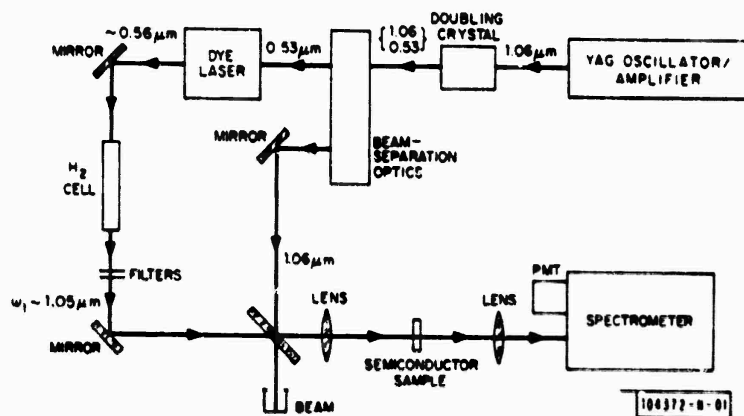
Fig. II-6. Experimental arrangement used for semiconductor CARS measurements.

provided by a 1.06-μm Q-switched YAG oscillator/amplifier. The output of this laser is also doubled to pump a dye laser operating around 560 nm. The output of the dye laser is then Raman shifted in a 33-atmosphere-pressure H_2-filled cell, and the second Stokes output from this cell is isolated using colored glass filters. The output is tunable from +530 cm^{-1} to −400 cm^{-1} around the 1.06-μm YAG output by tuning the dye laser, and thus provides the tunable source. The two beams are combined on a quartz beamsplitter and focused into the semiconductor material. The transmitted signal at the CARS frequency is isolated by a 3/4-m double-spectrometer and detected with a photomultiplier. The angle between the two beams may be adjusted to put the peak of the phase-matching curve in the spectral region of interest.

Figure II-7 shows GaAs LO phonon spectra at 300, 77, and 4.2 K taken using a 400-μm-thick Cr-doped semi-insulating sample. The laser beams were propagating along a [100] axis and were both polarized in a [110] direction. The background signal away from the phonon line is due to the nonresonant third-order susceptibility of GaAs. For the 300 K spectrum, an asymmetry due to interference between this nonresonant susceptibility and the resonant susceptibility due to the phonon is evident. At the lower temperatures, the background susceptibility is suppressed

17
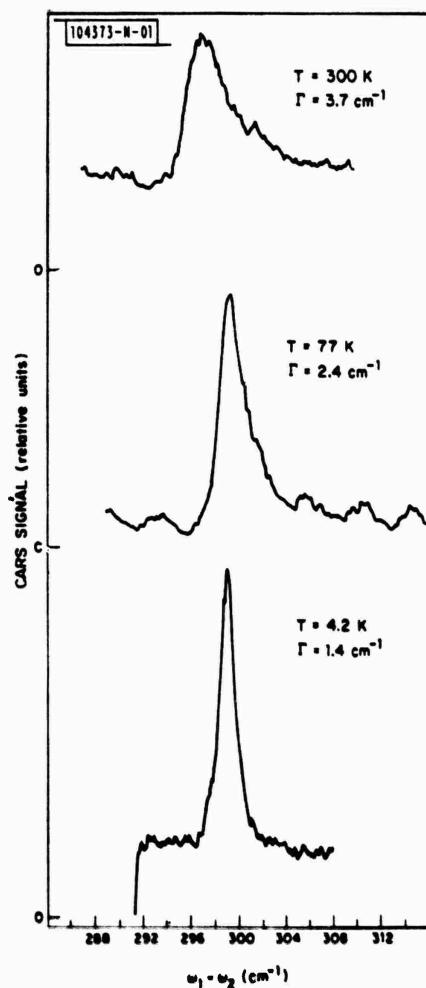
Fig. II-7. CARS measurement of LO phonon spectrum of GaAs at 300, 77, and 4.2 K. Linewidths are measured full-widths; spectral resolution set by laser bandwidths was approximately 0.5 cm^{-1}. 400-μm-thick GaAs material was Cr-doped semi-insulating substrate.

relative to the resonant susceptibility and this interference is not as distinct. The dominant source of the noise in these traces is due to instabilities in the laser sources. The signals were several orders of magnitude above detection sensitivity levels. Injection locking of the YAG and dye laser sources as well as normalization of the detected signals to a nonresonant background signal in another material should substantially improve the observed signal-to-noise ratios.

Experiments are currently in progress to extend these measurements to the detection of impurity transitions. In addition, Raman gain and RIKE measurements using a CW 1.15-μm He-Ne probe laser source are being investigated. The Raman gain technique is sensitive only to the imaginary part of the susceptibility, corresponding to energy absorption by the semiconductor, and is independent of nonresonant effects. The RIKE technique also suppresses the background susceptibility relative to the resonant terms. These experiments will provide a demonstration of the utility of nonlinear spectroscopic techniques as semiconductor diagnostic tools.

S. R. J. Brueck
H. Kildal

18

D. HIGHLY EFFICIENT LIQUID N$_2$ RAMAN LASER

Stimulated Raman scattering is a convenient technique for extending the available wavelength range of tunable lasers. Liquid N$_2$, due to its extremely high Raman gain and low coupling coefficients for competing nonlinear effects,[13] is a nearly ideal Raman laser medium and has been extensively studied.[14-16] We have investigated a single-pass liquid N$_2$ Raman laser using both tight-focusing and confocal geometries. In the confocal geometry, we find a quantum efficiency for conversion into the first Stokes component of 92 percent (80-percent energy-conversion efficiency). In the tight-focusing geometry, the input energy is distributed among a number of Stokes and anti-Stokes lines with only about 35-percent quantum efficiency for conversion to the first Stokes component. Further, we show that by proper choice of operating geometry it is possible to avoid the thermal lensing behavior at 10-Hz repetition rates that has been reported by other workers.[16]

The laser source for these experiments was a pulsed rhodamine 590 dye laser pumped by the second harmonic of a Q-switched Nd:YAG laser. The dye laser had a maximum output energy near 560 nm, an output spectral width of 0.3 cm^{-1}, and a pulse duration of 5 ns. For the tight-focusing experiments the dye laser radiation was focused to a 3.4-cm confocal parameter in a 10-cm optical path length cryogenic liquid dewar, while for the collimated-beam experiments the laser output was focused to a 165-cm confocal parameter in a 100-cm optical path length dewar. The forward scattered light was dispersed using KBr and SiO$_2$ prisms, and monitored using cross-calibrated pyroelectric energy meters. The backward Raman scattered light, which had only a first Stokes component, was monitored on reflection from a quartz beamsplitter.

Figures II-8 and II-9 show the input-output characteristics for the tight-focusing and collimated-beam geometries, respectively. For both geometries there is a substantial depletion
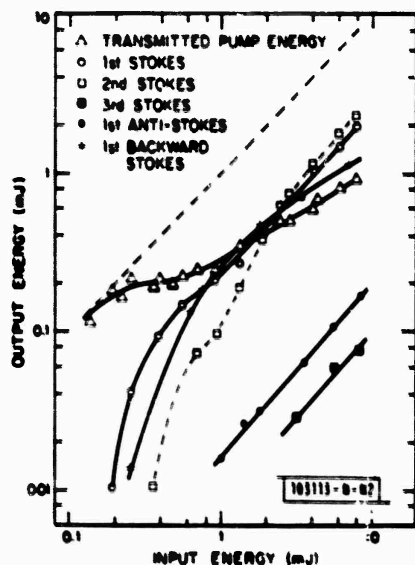
Fig. II-8. Output energies for stimulated Raman scattering in liquid N$_2$ in tight-focusing geometry (confocal parameter 3.4 cm, dewar path length 10 cm).
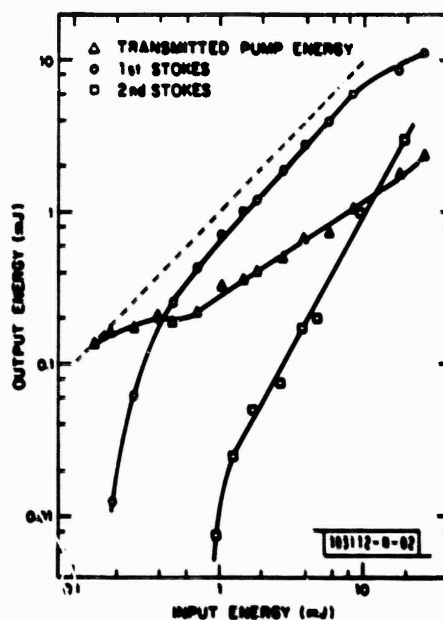
Fig. II-9. Output energies for stimulated Raman scattering in liquid N$_2$ in collimated-beam geometry (confocal parameter 165 cm, dewar path length 100 cm).

19
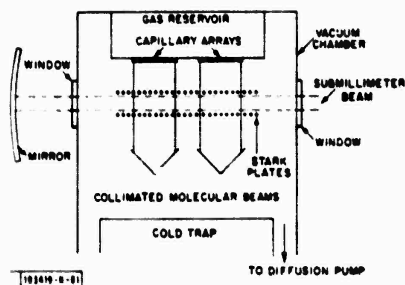
Fig. II-10. Molecular-beam apparatus showing capillary
arrays and Stark grids.
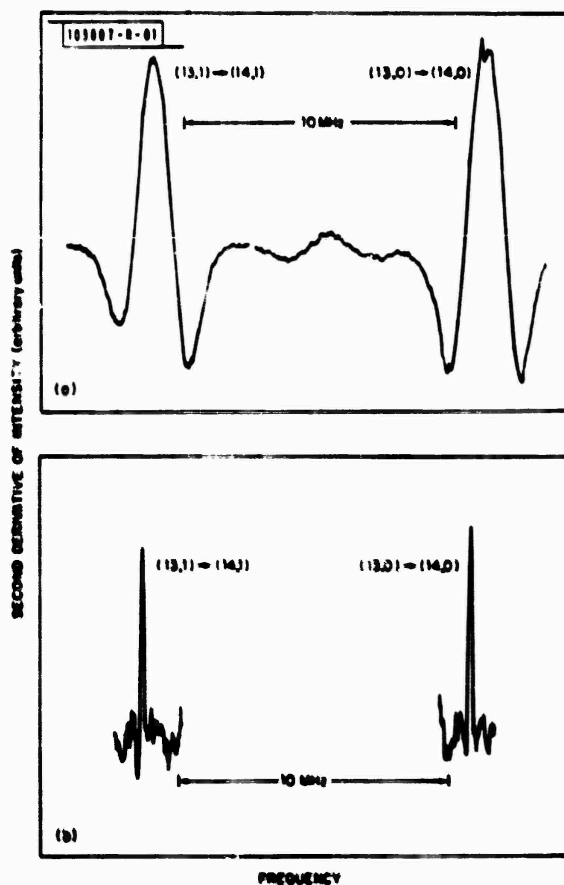
Fig. II-11. Second derivatives of (13,0) →
(14,0) and (13,1) → (14,1) rotational tran-
sitions of CH_3F at 714 GHz. (a) Doppler
line profile; (b) sub-Doppler line profile.

of the pump beam; the most notable difference between the two is that the conversion proceeds into many more Stokes and anti-Stokes components for the tight-focusing geometry. This limits the conversion efficiency into any one frequency. In contrast, for the collimated-beam geometry the coupling to higher-order scattering components is much weaker, and the quantum conversion efficiency into the first Stokes component is as high as 92 percent (80-percent energy-conversion efficiency). It should be stressed that these are not peak efficiencies but are averages over the entire pulse. The gain for backward-stimulated Raman scattering is much lower than the gain for forward scattering, since the pump laser spectral width of 0.3 cm^{-1} is larger than the N_2 Raman linewidth[13] of 0.067 cm^{-1} (cf. Refs. 14 and 17). Consistent with this, we did not observe any backward Raman scattering in the 100-cm cell. If the dye laser spectral width was narrowed to about 0.07 cm^{-1} by inserting an intracavity etalon, backward Raman scattering with an output critically dependent on the etalon tuning was observed. The forward scattering in this case was independent of the etalon adjustment. Contrastingly, in the 10-cm dewar, backward Raman scattering comparable in intensity to the forward scattering was always observed. The difference may be due to a reflective or scattering coupling between forward and backward waves, since the laser pulse duration was many dewar transit times in this case compared with only about 1.7 transit times for the longer dewar. The increased coupling to the higher-order Raman processes in the tight-focusing geometry may be due to four-wave mixing processes which are not present in the collimated-beam geometry due to dispersion and phase-matching considerations.

In both geometries the output divergences of the Raman beams were larger than that of the transmitted dye laser beam, and increased both with increasing pump level and increasing order. This spreading was present on the first pulse as well as on later pulses after a thermal steady-state had been achieved, and was due to off-axis Raman gain effects and not to the thermal lensing observed by Wild and Maier.[16]

<div align="right">

H. Kildal
S. R. J. Brueck
</div>

E. SUB-DOPPLER SUBMILLIMETER SPECTROSCOPY USING A MOLECULAR BEAM

The tunable sideband spectrometer described previously[18] has a frequency resolution on the order of 10 kHz. This resolution, which is two-orders-of magnitude smaller than the Doppler-limited linewidth of submillimeter molecular rotational transitions, has not previously been utilized for spectroscopy. Now, using a molecular-beam apparatus, sub-Doppler rotational lines at 700 GHz have been observed. As a demonstration of the frequency resolution of the system, the splitting between two closely spaced rotational lines at about 700 GHz has been measured to an accuracy of 70 kHz.

The width of the rotational lines is reduced below the Doppler limit by directing the submillimeter radiation through the molecular beam perpendicularly to the direction of flow of the molecular beam. The molecular-beam apparatus is of the type introduced by Chu and Oka[19] and applied by Pine and Nill,[20] in which the molecular beam is formed by a set of multitube glass capillary arrays. The capillary arrays produce well collimated molecular beams sufficiently dense to permit direct observation of the absorption of the tunable sideband radiation. As shown in Fig. II-10, the sideband radiation is double-passed through the molecular beam to increase the absorption length.

Absorption of the sideband radiation has been observed by frequency-modulating the sideband signal and synchronously detecting the second harmonic of the modulation frequency to obtain the second derivative of a rotational line. As is evident in Fig. II-11(a-b), which shows both

Doppler-limited and sub-Doppler rotational lines of CH_3F at 714 GHz, the linewidth of a transition observed with the molecular beam is an order-of-magnitude smaller than the Doppler-limited linewidth of an absorption in a cell. The lineshape and linewidth of the absorption due to the molecular beam depend upon the driving pressure in the gas reservoir behind the capillary array, which determines the transverse velocity distribution of the molecular beam. From the measured splitting of the $(J,K) = (13,0) \rightarrow (14,0)$ and $(13,1) \rightarrow (14,1)$ lines of CH_3F, the small centrifugal distortion constant H_{JK} is calculated to be 11 ± 6 Hz, which is consistent with the previous value of 8 ± 10 Hz (see Ref. 21).

Rotational transitions were also observed by Stark-modulating the absorptions and synchronously detecting the periodic component of the transmission of the sidebands. The molecular beam was directed through a pair of parallel, fine-mesh-wire grids, as indicated in Fig. II-10, and a square-wave voltage was applied across the grids. The $(J,K) = (13,3) \rightarrow (14,3)$ line of CH_3F obtained by Stark modulation is shown in Fig. II-12.
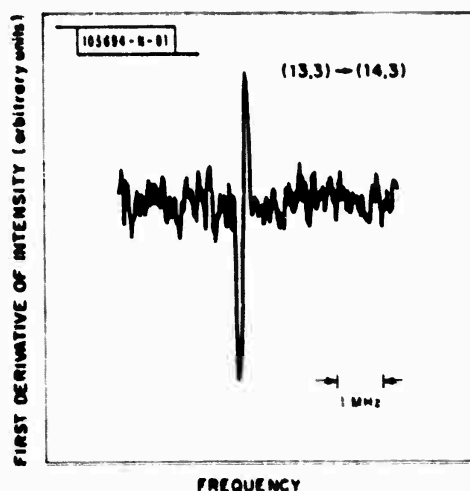
Fig. II-12. First derivative obtained by Stark modulation of $(13,3) \rightarrow (14,3)$ rotational transition of CH_3F at 714 GHz.

There are a number of interesting applications to spectroscopy and submillimeter laser technology of this submillimeter sideband, molecular-beam system. The absolute frequency of a molecular rotational line and the splittings between rotational lines clearly can be measured to extremely high accuracy. In addition, a submillimeter laser could be frequency-stabilized by offset-locking the laser to a suitable sub-Doppler rotational transition. Finally, the submillimeter laser could be locked directly to an optically pumped molecular beam of the lasing medium.

W. A. M. Blumberg
D. D. Peck
H. R. Fetterman

REFERENCES

1. Solid State Research Report, Lincoln Laboratory, M.I.T. (1980:2), pp. 11-12, DTIC AD-A092724.

2. D. K. Killinger and N. Menyuk, "DIAL Measurements of C_2H_4," Topical Meeting on Coherent Laser Radar for Atmospheric Sensing, Aspen, Colorado, 15-17 July 1980, Technical Digest paper ThC3.

3. N. Menyuk and P. F. Moulton, Rev. Sci. Instrum. 51, 216 (1980), DTIC AD-A085796/1.

4. B. Marthinsson, J. Johansson, and S. T. Eng, Opt. Quant. Electron. 12, 327 (1980).

5. J. A. Armstrong and A. W. Smith, Appl. Phys. Lett. 4, 196 (1964).

6. W. E. Ahearn and J. W. Crowe, IEEE J. Quantum Electron. QE-2, 597 (1966).

7. E. D. Hinkley and C. Freed, Phys. Rev. Lett. 23, 277 (1969), DDC AD-694147.

8. V. I. Annenkov, Yu. M. Mironov, V. I. Molochev, and A. S. Semenov, Sov. J. Quantum Electron. 8, 795 (1978).

9. M. Lax, in Physics of Quantum Electronics, edited by P. L. Kelley, B. Lax, and P. E. Tannenwald (McGraw-Hill, New York, 1966), p. 735.

10. M. W. Fleming and A. Mooradian (to be published in the IEEE Journal of Quantum Electronics).

11. H. Haug and H. Haken, Z. Phys. 204, 262 (1967).

12. V. F. Elesin and V. V. Rusakov, Sov. J. Quantum Electron. 5, 1239 (1976).

13. J. B. Grun, A. K. McQuillan, and B. P. Stoicheff, Phys. Rev. 180, 61 (1969).

14. S. A. Akhmanov, Yu. E. D'yakov, and L. I. Pavlov, Sov. Phys.-JETP 39, 249 (1974).

15. A. Z. Grasiuk, Appl. Phys. 21, 173 (1980).

16. E. Wild and M. Maier, J. Appl. Phys. 51, 3078 (1980).

17. M. G. Raymer, J. Mostowski, and J. L. Carlsten, Phys. Rev. A 19, 2304 (1979).

18. W. A. M. Blumberg, H. R. Fetterman, D. D. Peck, and P. F. Goldsmith, Appl. Phys. Lett. 35, 582 (1979), DDC AD-A084590/9; Solid State Research Reports, Lincoln Laboratory, M.I.T. (1979:3), p. 28, DDC AD-A084270/8, and (1979:1), p. 30, DDC AD-A073152/1.

19. F. Y. Chu and T. Oka, J. Appl. Phys. 46, 1204 (1975); F. Matsushima, N. Morita, S. Kano, and T. Shimizu, J. Chem. Phys. 70, 4225 (1979).

20. A. S. Pine and K. W. Nill, J. Mol. Spectrosc. 74, 43 (1979), DDC AD-A070126/8.

21. E. Arimondo and M. Inguscio, J. Mol. Spectrosc. 75, 81 (1979).

A. ORIENTATION-DEPENDENT GROWTH OF InP BY VAPOR-PHASE EPITAXY

In a study of the vapor-phase-epitaxial (VPE) growth of InP layers on single-crystal InP substrates by the PCl_3-InP-H_2 method, we have demonstrated that under suitable experimental conditions the growth rate varies significantly with crystallographic orientation. The relative growth rates on the principal low-index planes have been determined, and the orientation dependence has been utilized to obtain structures in which single-crystal InP layers are grown laterally over phosphosilicate glass (PSG) films. Structures of this type are of potential interest as waveguides for infrared radiation in integrated optical circuits. This study was motivated by the recent success of Bozler and coworkers in using the analogous $AsCl_3$-GaAs-H_2 method to obtain high-quality GaAs layers by lateral growth over SiO_2 films[1] and other foreign materials.

Deposition of InP by the PCl_3-InP-H_2 process was carried out in an open-tube reactor. In this process, PCl_3 vapor is first reacted with H_2 at high temperature to form a gaseous mixture of P_4 and HCl. Next, this mixture reacts with an InP source at high temperature to produce a gaseous mixture of InCl, P_4, and H_2. Finally, the second reaction is reversed at a lower temperature, causing deposition of InP on the substrate. Figure III-1 shows a schematic diagram of the reactor, together with a representative temperature profile. High-purity poly-crystalline InP, synthesized from the elements in our laboratory, then cleaned and etched, was used as the source material. The substrates were oriented, polished, and etched wafers cut from crystals grown in our laboratory by the LEC technique. They were mounted with their broad surfaces — which are either (111), (110), or (100) planes — parallel to the gas flow. All four sides of the (100) substrates are cleaved (110) faces, while the other substrates have one pair of cleaved (110) sides.
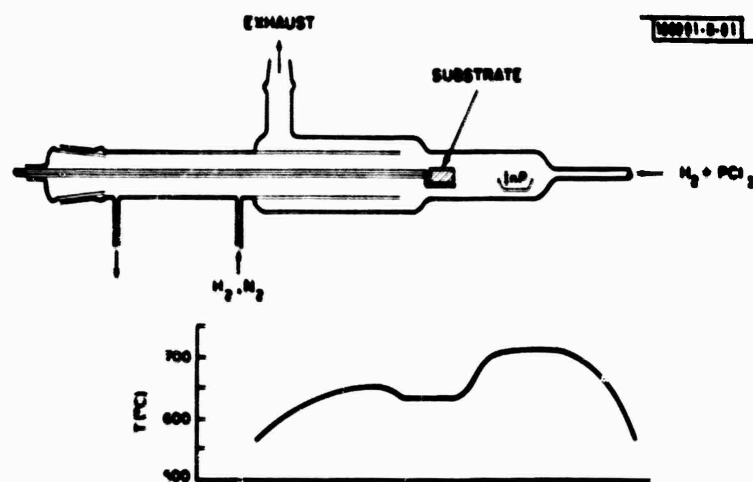

Fig. III-1. Schematic diagram of reactor and temperature profile for growth of InP by vapor-phase epitaxy.
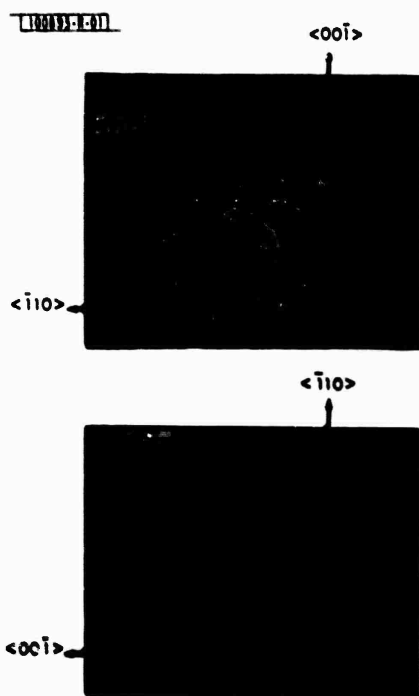
Fig. III-2. Photomicrograph of cleaved and stained end section of InP layer grown on (100) InP substrate.
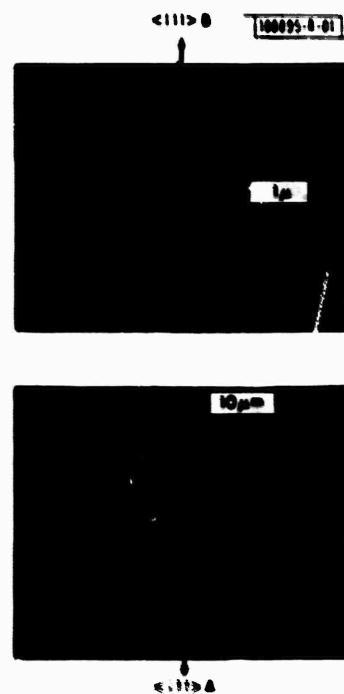
Fig. III-3. Photomicrograph showing difference in InP growth rates on opposite faces of (111) substrate.

In order for the growth rate of VPE layers to vary with crystallographic orientation, deposition must take place under kinetic control, which is a consequence of differences in surface energy associated with differences in surface structure. The orientation dependence is therefore enhanced by growth at low temperatures and at low rates (i.e., at low values of gas phase supersaturation). In our experiments, we have deposited InP layers at temperatures as low as 500°C and at rates as low as 0.2 μm/h.

In one series of experiments, we investigated the relative growth rates on the principal low-index planes. For this purpose we employed two techniques that involve simultaneous growth on at least two different planes in a single run. Such techniques are necessary because the kinetically controlled growth of InP depends so strongly on the specific experimental conditions, that reliable comparisons cannot be made between rates on different planes measured in different runs, even though the conditions are nominally the same. An important source of the run-to-run variation at low growth rates is the etching of the substrate and the growing layers by HCl that is present in the gas phase because of its incomplete reaction with the InP source or its recirculation after being liberated by the deposition reaction. In some cases, this etching can even result in net removal of the substrate rather than growth. Under the conditions of our experiments, we have found that the HCl etching rates for the principal low-index orientations decrease in the order (110) > (111)A > (100) > (111)B.

One of the techniques used for determining relative growth rates was to mount two substrates with different orientations side-by-side in the reactor, carry out a growth run, and then measure the thickness of the epilayer deposited on each substrate. The second technique was to compare the thickness of layers grown on differently oriented surfaces of a single substrate. In applying this technique, growth was carried out on semi-insulating (100) and (111) substrates, which were cleaved after growth to expose a (110) face parallel to the growth directions. To determine the epilayer thickness, the cleaved face was stained with an aqueous solution of potassium ferricyanide and potassium hydroxide. Since the etching action of this solution depends on the InP carrier concentration, the solution delineates the interface between the substrate and the epilayer, which is much higher in carrier concentration than the substrate.

The results obtained by the second technique are illustrated by Figs. III-2 and III-3. Figure III-2 is a photomicrograph showing one corner of the cleaved and stained end of a (100) substrate after epilayer growth. This corner contains a quadrant of all the orientations between the ⟨110⟩ and ⟨001⟩ directions. The thickness is seen to be about four times greater for growth on the (110) side of the substrate than for growth on the (001) face, and a very prominent (111)A facet has been formed. The interfaces between the facet and the (110) and (001) growths have been stained by the etch, showing that different carrier concentrations were obtained for growth in the different directions. Figure III-3 is a photomicrograph showing the difference in the thickness of the layers grown on the opposite faces of a (111) substrate as revealed by cleaving and staining. The growth rate on the (111)A face is more than ten times greater than the rate on the (111)B face.

As pointed out previously, the rates of kinetically controlled growth are extremely sensitive to the experimental conditions. Even the ratios of the growth rates in different crystallographic directions are sensitive to the experimental conditions, although to a considerably lesser degree. Therefore, to obtain significant values of these ratios for the principal low-index directions, we have used the techniques described to perform about twenty experiments under a narrow range of experimental conditions that gave growth rates in the ⟨111⟩B direction of 0.2 to

TABLE III-1
InP GROWTH RATES

Direction	Relative Growth Rates
⟨110⟩	60
⟨100⟩	15
⟨111⟩A	12
⟨111⟩B	1

0.5 μm/h.   The results obtained by the two techniques are consistent.   Table III-1 gives the values obtained for the relative growth rates.   The rate decreases in the order ⟨110⟩ > ⟨100⟩ > ⟨111⟩A > ⟨111⟩B.   In an earlier investigation, Mizuno[2] studied deposition of InP by the trichloride technique at growth rates up to 70 μm/h.   For rates below about 20 μm/h, he did not observe any dependence of rate on substrate orientation.

In another series of experiments, we have shown the feasibility of utilizing the dependence of VPE growth rates on crystallographic direction to obtain single-crystal InP layers over PSG films.   In these experiments, a thin film of PSG is deposited on an InP substrate and narrow stripes are opened in the film by photolithographic techniques.   Depending on the orientation and growth conditions, vertical epitaxial growth initiated on the InP surface exposed through the
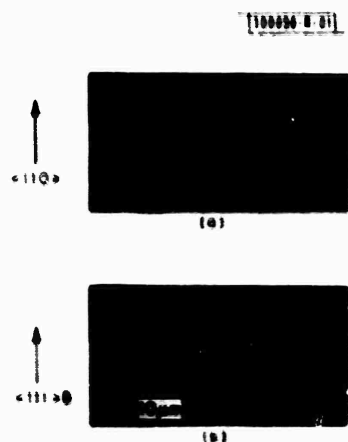
Fig. III-4.   Photomicrographs of (110) cleavage sections showing asymmetrical lateral overgrowth of InP.   (a) (110) substrate;   (b) (111)B substrate.
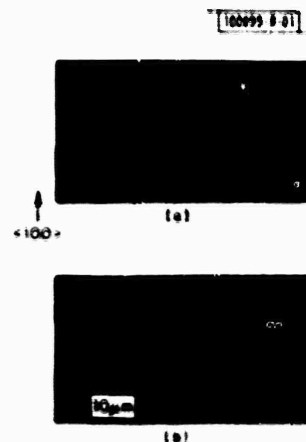
Fig. III-5(a-b).   Photomicrographs of (110) cleavage sections showing lateral growth of InP over PSG film on (100) InP substrate.

stripe openings can be followed by significant lateral growth over the PSG film.   Figure III-4(a-b) shows cleaved cross sections of samples for which lateral growth took place over PSG films deposited on (110) and (111)B substrates.   For the orientations used, the lateral growth is highly anisotropic.   Figure III-5(a-b) shows two cleaved cross sections for a sample with (100) substrate orientation.   In this case, the lateral growth is symmetric.   In Fig. III-5(b) it is seen that

lateral growth initiated at two adjacent stripe openings has been sufficient to form a continuous InP layer completely covering the PSG film.

P. Vohl

B. TRANSITION TEMPERATURES AND HEATS OF CRYSTALLIZATION OF AMORPHOUS Ge, Si, AND $Ge_{1-x}Si_x$ FILMS

Amorphous films in the Ge-Si system, as well as films prepared by their transition to the crystalline state, are of current interest as materials for potential device applications. For example, solar cells with conversion efficiencies as high as 6 percent at AM1 have been fabricated from a-Si:H films,[3] and a-$Ge_{1-x}Si_x$ cells are being investigated[4] in order to obtain a better match to the solar spectrum. Numerous studies have been made on energy-beam annealing and crystallization of a-Si (see Ref. 5) and a-Ge (see Refs. 6 and 7) films deposited on various substrates. These studies have found that both the amorphous-to-crystalline transition temperature T_t and the latent heat of crystallization ΔH play major roles in crystallization dynamics.

In the investigation reported here, we have used differential scanning calorimetry (DSC) to measure the values of T_t and ΔH for a-Ge, a-Si, and a-$Ge_{1-x}Si_x$ alloy films prepared by RF sputtering. Our measurements show that both T_t and ΔH (per gram) increase linearly with x in the alloy system.

Amorphous films a few micrometers thick were deposited on fused silica substrates by sputtering in purified Ar. The sputtering system contained two polycrystalline targets, one Ge and the other Si. The substrates were mounted on a water-cooled stainless-steel platform. To prepare $Ge_{1-x}Si_x$ films, the two targets were sputtered simultaneously, and the platform was rotated at 10 rpm so that each substrate alternately intercepted the sputtered beam arising from each target. The alloy composition was adjusted by changing the target sputtering rates. Typically, the deposition rate of each element was varied from 10 to 30 Å/min. The substrate rotation speed and the deposition rates were such that the alloy films comprised an intimate mixture of Ge and Si, rather than discrete layers of the two constituents. Pure Ge and Si films were prepared by sputtering only one target, with or without platform rotation. The deposition rates were found to be about eight times slower with rotation than without it.

About a dozen substrates 2.5 × 2.5 cm square were coated during a single deposition run. The substrates were then soaked in HF for several days, during which the sputtered films floated off in flakes that were usually sufficient to provide samples for many DSC measurements. The measurements were performed with a commercial calorimeter provided with independently heated sample and reference chambers. To make a DSC run, the sample chamber was loaded with amorphous flakes having a total weight of a few milligrams, which were sandwiched between two disposable copper crucibles that had been coated with Al_2O_3 to prevent interaction with the flakes. The two chambers were then heated under Ar, using heat inputs automatically adjusted to raise the temperatures of both chambers at the same constant rate, and the instantaneous difference between the two heat inputs was plotted as a function of temperature.

Figure III-6 shows typical DSC traces of differential heat input vs temperature obtained at a heating rate of 10°C/min. for a-Ge and a-Si samples deposited with platform rotation. The a-Ge trace contains a single exothermic peak resulting from the release of latent heat during crystallization. The value of T_t, taken as the temperature at which the line of maximum gradient intersects the baseline, is 501°C. The value of ΔH, which was determined by using calibration data from a measurement of the specific heat of a sapphire crystal, is 39.8 cal/g.
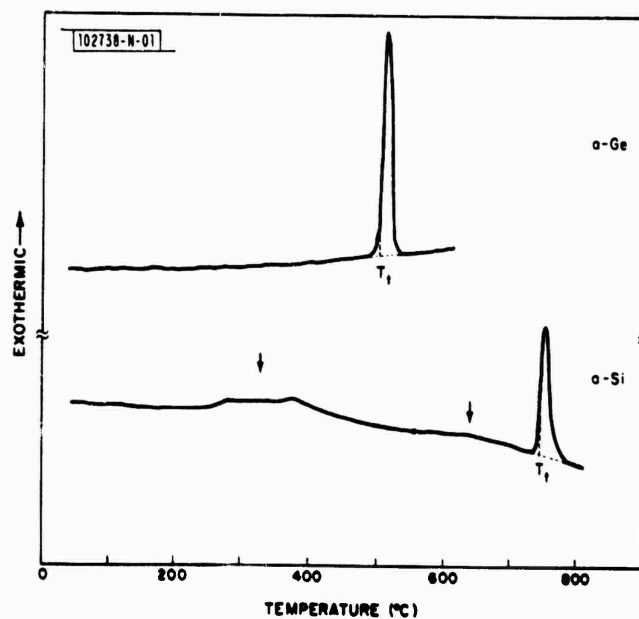
Fig. III-6. Typical DSC traces for crystallization of a-Ge and
a-Si films deposited with platform rotation.
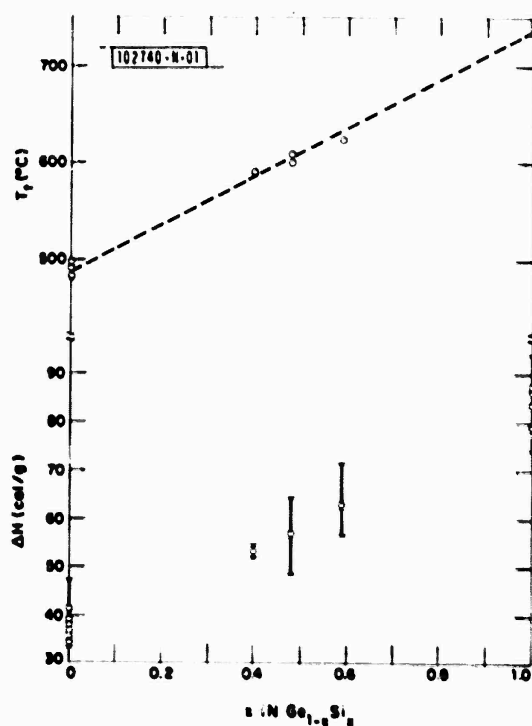
Fig. III-7. Transition temperature
T_t (upper plot) and heat of crystal-
lization ΔH (lower plot) as a func-
tion of x for amorphous $Ge_{1-x}Si_x$
films.

The a-Si trace in Fig. III-6 contains a small, broad exothermic feature at 300° to 400°C and another small exothermic feature at about 600°C, in addition to the main crystallization peak, for which T_t = 741°C and ΔH = 80.9 cal/g. For each of the a-$Ge_{1-x}Si_x$ films the DSC trace also contains one major peak, with T_t intermediate between the values for a-Ge and a-Si, and a small, broad exothermic feature near 300°C, but none near 600°C. The small feature probably resulted from a reordering of the amorphous configuration, since x-ray diffractometer data do not reveal any crystalline material for films that have been heated at 10°C/min. to temperatures just below T_t. The occurrence of only one major DSC peak for the a-$Ge_{1-x}Si_x$ films indicates that these films were deposited as alloys rather than as mixtures of discrete a-Ge and a-Si phases. This conclusion is supported by x-ray diffractometer data for crystallized $Ge_{1-x}Si_x$ films, which show that each consists of a single phase with lattice constant intermediate between those of Ge and Si.

In preliminary DSC experiments on a-Ge films, we found that T_t depends on the heating rate, as expected for the transformation of a metastable phase to the stable form. The values of T_t measured at a rate of 5°C/min. were 10° to 15°C lower, and those measured at 20°C/min. were 10° to 15°C higher, than the values obtained at 10°C/min. The data reported here were obtained in runs at 10°C/min. The values of ΔH measured for a-Ge did not depend on the heating rate over the range from 5° to 20°C/min., indicating that at these rates no significant crystallization occurred before the onset of the exothermic peak.

The upper plot in Fig. III-7 shows T_t as a function of x for the $Ge_{1-x}Si_x$ system. Each point represents the average of the T_t values measured for all samples prepared in one deposition run. For each run, these values agreed within a few degrees. The data show that T_t increases linearly with x from about 490°C for Ge to 740°C for Si. The x values for the three alloys were determined by Auger spectroscopy before crystallization. They are consistent with the values determined from the lattice constants measured by x-ray diffraction after crystallization.

The lower plot in Fig. III-7 shows ΔH (in cal/g) as a function of x. Each point represents the average of the ΔH values measured for all the samples from a single deposition run. The relative range of values obtained for each deposition run is considerably larger for ΔH than for T_t. The spread in ΔH for all samples with the same x value is indicated in the figure. Within the experimental uncertainty, the data are consistent with a linear variation of ΔH with x from about 37 cal/g for a-Ge to about 85 cal/g for a-Si. These values correspond to 2.7 kcal/mol for a-Ge and 2.4 kcal/mol for a-Si. Our value for a-Ge falls within the range of reported experimental values,[8-11] and is close to the theoretical value of 3.1 kcal/mol calculated by Grigorovici and Manaila.[12] The linear dependence of T_t and ΔH (in cal/g) on x may be related to the fact that Ge and Si are totally miscible in the crystalline state, and also may indicate that a-Ge and a-Si have similar configurations. The reasonably large values of ΔH for a-$Ge_{1-x}Si_x$ and a-Si suggest that these materials may exhibit the "explosive" crystallization observed[6,13] for a-Ge.

After background subtraction, the major exothermic peaks in Fig. III-6 are found to have Gaussian shapes. However, for a-Si and a-Ge films prepared in deposition runs during which the sample platform was not rotated, the major peaks have two components. (Double peaks were not observed for the a-$Ge_{1-x}Si_x$ films, which were prepared with platform rotation.) Preliminary experiments suggest that these components may be due to the crystallization of two

amorphous phases with different configurations and slightly different transition temperatures. The presence of two phases in the films deposited without substrate rotation could be associated with the much higher deposition rates and probable reduction in trapped gas content.

J. C. C. Fan
C. H. Anderson, Jr.

C. SOLID-PHASE HETEROEPITAXY OF Ge ON ⟨100⟩ Si

We have utilized GaAs epilayers grown by chemical vapor deposition (CVD) on single-crystal Ge substrates to fabricate thin-film GaAs solar cells with conversion efficiencies up to 21 percent (AM1).[14] A marked reduction in cost is expected if such cells can be fabricated on Si substrates, but high-quality GaAs has not been obtained by direct growth on Si. To prepare such material, we have proposed[14,15] that a graded heteroepitaxial $Ge_{1-x}Si_x$ alloy be used as an interlayer between the GaAs and Si. We have recently prepared $Ge_{1-x}Si_x$ films on Si by transient heating of Ge-coated Si single-crystal substrates to 950° to 1000°C on a graphite strip-heater.[16] These films are of good crystal quality, but they exhibit surface roughness that imposes some difficulties in the subsequent growth of GaAs epilayers.

Here, we describe an alternative approach to the problem of growing GaAs on Si. Instead of preparing $Ge_{1-x}Si_x$ films, we have used solid-phase epitaxy (SPE) to obtain smooth heteroepitaxial Ge films by crystallization of amorphous Ge deposited on single-crystal Si substrates. We have then grown good-quality GaAs heteroepitaxial layers by CVD on the SPE Ge films. Solid-phase heteroepitaxy of Ge on ⟨100⟩ Si has recently been observed,[17] but it has not been reported in the literature.

Germanium films 1000 to 3000 Å thick were deposited by electron-beam evaporation of high-purity Ge on ⟨100⟩ Si substrates. The Si wafers were cleaned by conventional procedures and rinsed with dilute (10 percent) HF immediately prior to loading into the oil-diffusion-pumped vacuum system. They were not intentionally heated or cooled during deposition. The average deposition rate was about 8 Å/s. The Ge/Si ⟨100⟩ samples were heat-treated in a quartz-tube furnace or on a graphite strip-heater with flowing forming gas (Ar/H_2) ambient. In each experiment, annealing was carried out for 15 min. at a constant temperature in the 650° to 750°C range.

X-ray and reflection high-energy-electron-diffraction (RHEED) measurements showed that the as-deposited Ge films were amorphous, whereas the annealed films were single crystalline. The SPE Ge films exhibited smooth surface morphology indistinguishable from that of as-deposited films. Figure III-8(a) is the (011) RHEED pattern of a typical SPE Ge film 2000 Å thick. The pattern contains strong matrix spots streaked along the ⟨011⟩ azimuth direction, indicating that the film is epitaxial and has a rather smooth surface. Additional weak satellite spots are present due to {111} twinned regions of the crystal. Faint traces of polycrystalline rings were occasionally detected for the 3000-Å-thick Ge films, but most of the thinner films did not give polycrystalline reflections.

The RHEED patterns were generated by diffraction from a region estimated to be a few hundred angstroms deep. To study the crystal quality of the SPE films as a function of depth, several films were chemically etched in steps of ~400 Å and re-examined by RHEED after each etch. The RHEED patterns showed a slight decrease in twin diffraction intensities with successive etching steps, and polycrystalline diffractions were completely absent after etching. These

Fig. III-8. RHEED patterns for heteroep-
itaxial Ge films obtained by solid-phase
crystallization of amorphous Ge films de-
posited on ⟨100⟩ Si single-crystal sub-
strates. (a) After initial annealing at
700°C for 15 min. (b) After subsequent
implantation of Ga^+ ions and reannealing
at 700°C for 15 min.
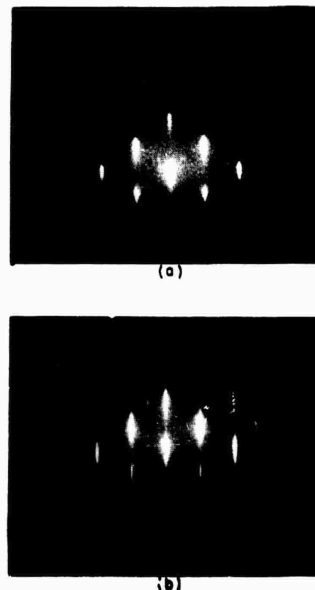
results indicate that, with respect to twins and random polycrystallites, the crystal quality of
the SPE Ge films increases gradually toward the Ge-Si interface. However, transmission elec-
tron microscopy (TEM) revealed, in addition to twins, a dense network of misfit dislocations
at the Ge-Si interface as well as some inclined dislocations propagating up toward the surface.

Our results demonstrate that epitaxial growth of Ge on Si can be accomplished by solid-
phase crystallization in spite of the 4-percent lattice mismatch between the two materials. The
polycrystallinity occasionally observed near the film surface can be attributed to either surface-
or impurity-induced nucleation.[18] Increasing the film thickness increases the probability of such
random nucleation, which may occur before ordered transformation is completed by the crys-
tallization front advancing from the film-substrate interface.

We have significantly improved the crystal quality of SPE Ge films by employing a technique
suggested by the fact that solid-phase homoepitaxy of Ge (see Ref. 19) and Si (see Refs. 20 through
22) has been used to convert amorphous surface layers to high-quality crystalline material.
Following the initial SPE anneal, the Ge film was implanted at liquid nitrogen temperature with
Ga^+ ions, using an ion energy and dose selected to produce an amorphous upper layer about
two-thirds the total thickness of the film. The Ge/Si sample was then reannealed at 700°C for
15 min., causing the amorphous upper layer of the Ge film to recrystallize by solid-phase homo-
epitaxy, which was seeded by the lower region of the film that had not been damaged by ion im-
plantation. After reannealing, the film surface was just as smooth as it had been for the as-
deposited film.

Figure III-8(b) is the RHEED pattern obtained for an SPE Ge film after ion implantation and
reannealing. In comparison with the pattern of Fig. III-8(a), the principal diffraction spots are
sharper and more elongated, the spots due to (111) twins have disappeared, and the Kikuchi lines
are stronger. All these features are evidence for a marked improvement in crystal quality at
the surface. The improvement has been confirmed by TEM observations, which showed that

twins were no longer present in the upper layer of the film after reannealing, although disloca-
tions were still present throughout the film.

The improvement in crystal quality has also been confirmed by the results of channeling
experiments with 1.0-MeV ^{4}He$^+$ ions. Figure III-9(a-b) shows the channeling spectra for
2000-Å-thick Ge films on $\langle 100 \rangle$ Si after the initial SPE anneal [Fig. III-9(a)] and after the im-
plantation and reannealing treatment [Fig. III-9(b), which also shows the spectrum for a polished
$\langle 100 \rangle$ Ge single-crystal wafer]. The implantation-reannealing treatment results in a decrease
of the minimum surface yield for the SPE film from 18 percent in Fig. III-9(a) to 4.5 percent in
III-9(b). After this treatment, the spectrum for the near-surface region of the film is almost
the same as that for the Ge single-crystal wafer. Neither of the spectra in Fig. III-9 reveals
any broadening of the interface between the Ge film and the Si substrate. The observed sharp-
ness of the interface is consistent with solid-phase crystallization, rather than crystallization
involving the formation of a liquid phase.

Our characterization results show that after ion implantation and reannealing, the near-
surface region of the SPE Ge films is higher in crystal quality than this region in the $Ge_{1-x}Si_x$
alloy films prepared by transient heating of Ge-coated Si substrates on a graphite strip-heater.
Thus, the minimum surface yield obtained in channeling experiments is 6 to 8 percent for the
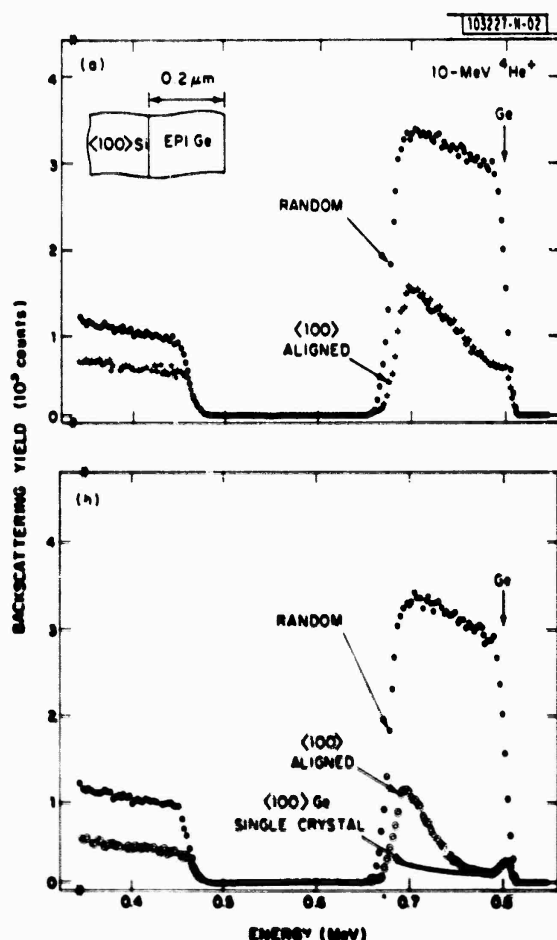
Fig. III-9. ^{4}He$^+$ ion channeling spectra
for SPE Ge/Si$\langle 100 \rangle$ samples: (a) after
initial annealing; (b) after subsequent
implantation and reannealing. RHEED
patterns of SPE Ge films are shown in
Figs. III-8(a) and (b), respectively.

alloy films,[16] compared with 4.5 percent for the Ge films after the implantation-reannealing treatment.

As an initial step in determining the usefulness of SPE Ge films as substrates for the growth of GaAs, undoped GaAs epitaxial layers about 2 μm thick were grown by CVD on SPE Ge films that had been subjected to the implantation-reannealing treatment. Details of the deposition procedure have been described elsewhere.[23] The GaAs layers were found to be at least comparable, and in most cases superior, in crystal quality to the underlying Ge films. Figure III-10

Fig. III-10. ^{4}He$^+$ channeling spectrum for GaAs layer about 2 μm thick grown by CVD on a SPE Ge/Si⟨100⟩ substrate after ion implantation and reannealing.
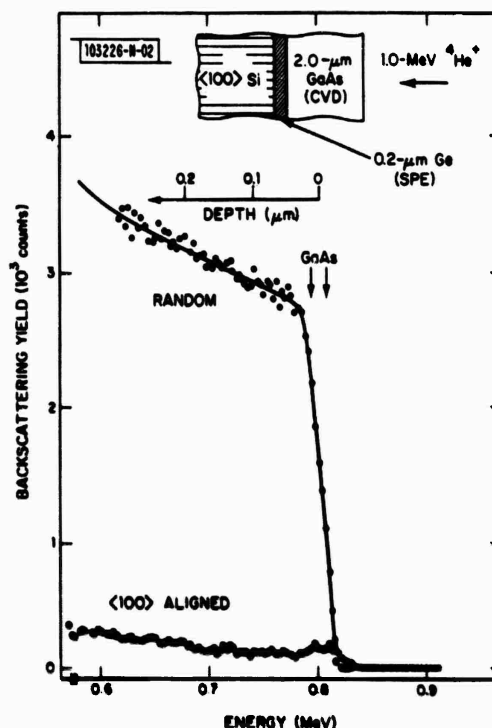
shows the 1.0-MeV ^{4}He$^+$ channeling spectrum of one of the GaAs layers. The minimum surface yield is only about 4 percent, indistinguishable within the experimental uncertainty from that of a polished GaAs single crystal. On the basis of this result, it appears highly probable that GaAs layers suitable for the fabrication of high-efficiency thin-film solar cells can be grown on SPE Ge/Si substrates.

B-Y. Tsaur
J.C.C. Fan
R. P. Gale

REFERENCES

1. F. J. Leonberger, C. O. Bozler, R. W. McClelland, and I. Melngailis, "Oxide-Confined GaAs Optical Waveguides Formed by Lateral Epitaxial Growth," Topical Meeting on Integrated and Guided-Wave Optics, Incline Village, Nevada, 28-30 January 1980, Technical Digest, pp. WB1-1–WB1-4.

2. O. Mizuno, Jpn. J. Appl. Phys. $\underline{14}$, 451 (1975).

3. D. E. Carlson and C. R. Wronski, Appl. Phys. Lett. $\underline{28}$, 671 (1976); D. E. Carlson, IEEE Trans. Electron. Devices $\underline{ED-24}$, 449 (1977).

4. V. L. Dalal and E. A. Fagen, Conference Record of the 14th IEEE Photovoltaic Specialists Conference, San Diego, California, 1980 (IEEE, New York, 1980), p. 1066.

5. For example, see J. C. C. Fan and H. J. Zeiger, Appl. Phys. Lett. $\underline{27}$, 224 (1975), DDC AD-A016696/7; M. W. Geis, D. C. Flanders, and H. I. Smith, Appl. Phys. Lett. $\underline{35}$, 71 (1979), DDC AD-A076745/9; J. F. Gibbons, K. F. Lee, T. J. Magee, J. Peng, and R. Ormond, Appl. Phys. Lett. $\underline{34}$, 831 (1979).

6. J. C. C. Fan, H. J. Zeiger, R. P. Gale, and R. L. Chapman, Appl. Phys. Lett. $\underline{36}$, 158 (1980), DTIC AD-A090909.

7. For example, R. B. Gold, J. F. Gibbons, T. J. Magee, J. Peng, R. Ormond, V. R. Deline, and C. A. Evans, Jr., Proceedings, Laser-Solid Interactions and Laser Processing (Academic Press, New York, 1980), p. 221; G. H. Gilmer and H. J. Leamy, ibid., p. 227; S. S. Lau, W. F. Tseng, M-A. Nicolet, J. W. Mayer, J. A. Minnucci, and A. R. Kirkpatrick, Appl. Phys. Lett. $\underline{33}$, 235 (1978).

8. H. S. Chen and D. Turnbull, J. Appl. Phys. $\underline{40}$, 4214 (1969).

9. M. L. Rudee, Thin Solid Films $\underline{12}$, 207 (1972).

10. R. J. Temkin and W. Paul, Amorphous and Liquid Semiconductors, J. Stuke and W. Brenig, Eds. (Taylor and Frances, London, 1974), p. 1193.

11. H. S. Randhawa, L. K. Malhotra, H. K. Sehgal, and K. L. Chopra, Phys. Status Solidi A $\underline{37}$, 313 (1976).

12. R. Grigorovici and R. Manaila, Nature (London) $\underline{226}$, 143 (1970).

13. T. Takamori, R. Messier, and R. Roy, Appl. Phys. Lett. $\underline{20}$, 201 (1972).

14. J. C. C. Fan, C. O. Bozler, and B. J. Palm, Appl. Phys. Lett. $\underline{35}$, 875 (1979), DDC AD-A085501/5.

15. J. C. C. Fan, G. W. Turner, R. P. Gale, and C. O. Bozler, "GaAs Shallow-Homojunction Solar Cells," Proc. Fourteenth IEEE Photovoltaic Specialists Conference – 1980, San Diego, California, 7-10 January 1980, pp. 1102-1105, DTIC AD-A090668.

16. J. C. C. Fan, R. P. Gale, F. M. Davis, and G. Foley, Appl. Phys. Lett. (in press).

17. I. S. Hung and S. S. Lau, personal communication.

18. K. Zellama, P. Germain, S. Squelard, J. C. Bourgoin, and P. A. Thomas, J. Appl. Phys. $\underline{50}$, 6995 (1979).

19. L. Csepregi, R. P. Kullen, and J. W. Mayer, Solid State Commun. $\underline{21}$, 1019 (1977).

20. J. A. Roth and C. L. Anderson, Appl. Phys. Lett. $\underline{31}$, 689 (1977).

21. J. C. Bean and J. M. Poate, Appl. Phys. Lett. $\underline{36}$, 59 (1980).

22. M. von Allmen, S. S. Lau, J. W. Mayer, and W. F. Tseng, Appl. Phys. Lett. $\underline{35}$, 280 (1979).

23. C. O. Bozler, J. C. C. Fan, and R. W. McClelland, "Efficient GaAs Shallow-Homojunction Solar Cells on Ge Substrates," Chapter 5 in Gallium Arsenide and Related Compounds (St. Louis) 1978 (The Institute of Physics, London, 1979), pp. 429-436, DDC AD-A072370/0.

IV. MICROELECTRONICS

A. CHARGE-COUPLED DEVICES: IMAGERS

The 100- × 400-element CCD imager for the GEODSS (Ground Electro-Optical Deep Space Surveillance) program must have high performance down to very low signal levels. Previously, we demonstrated low-noise operation of the CCD output charge-detection circuit, obtaining noise levels of 10 electrons.[1] To complete the low-light-level characterization of the device, we have measured the charge transfer inefficiency for charge packet sizes spanning the dynamic range of the device. Such measurements are described here, and the results show negligible charge loss for charge packets ranging from 100 to 500,000 electrons.

The standard method of measuring charge transfer loss in a CCD is to launch several equal-sized charge packets in succession into the CCD. At the output, the first charge packet will generally be lower in amplitude. This charge loss is called charge transfer inefficiency (CTI). Unless the charge loss is very large, the second or third and all subsequent packets will be loss-free since any charge they lose will be balanced by charge they acquire from packets that precede them. The charge loss of the first packet is the parameter we use to characterize the CTI of the 100- × 400-element imager.

As described in a prior report,[2] this device is a 400-column by 100-row imager with both input and output registers so that it can be operated as a serial-parallel-serial delay line. CTI must be measured for the 402-stage output register operating at 400 kHz, and for each of the 100-stage imaging registers operating at 1 kHz. These measurements have been made for charge packet sizes spanning the entire usable dynamic range of the device. However, low-charge-level CTI measurements are the most critical for the GEODSS application, and they are also more likely to reveal areas of poor charge transfer because bulk trapping in a buried-channel device has a disproportionately larger effect on small packets than on large ones. Also, we have observed a new charge loss mechanism which we observe only at low charge levels, and this mechanism is discussed below.

An example of excellent performance at low-signal levels with the device cooled to $-50°C$ is shown in Fig. IV-1. Three groups of three charge packets, each about 110 electrons, are launched into the input register and transferred to three adjacent columns of the imaging section where they are transported down to the output register and out to the charge-detection circuit. The timing is arranged so that the three charge packets in each column are contiguous, as diagrammed in Fig. IV-1. The three photographs in the figure show the output signals from the device for each group. Any charge loss in the serial input or output registers would be revealed by a decreased amplitude in the first signal in each photograph, whereas charge loss in the column registers would result in a lower amplitude of a signal in the first photograph relative to the same signals in the second and third photographs. Because the signals are close to the device noise limit of 10-rms electrons, each photograph was time-exposed to record about 200 signals. This provides a time-averaging effect so that the signal amplitudes can be more easily estimated. The photographs of Fig. IV-1 show that any charge loss, if present, is less than about 10 percent or 11 e^-. This amounts to a CTI of better than 1.0×10^{-4} per transfer for the 1,008 transfers. For larger charge packets, where the signal/noise is larger, the CTI was measured to be less than 1×10^{-5} up to a maximum charge capacity of 500,000 e^- per pixel.
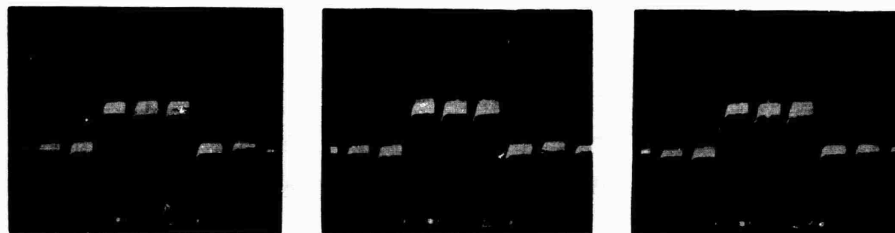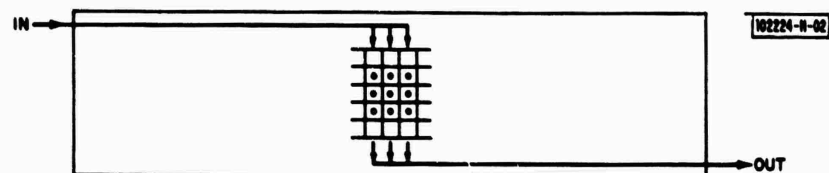
Fig. IV-1. Demonstration of low-signal charge transfer inefficiency. Nine charge packets, each about 110 electrons, are shown after 1008 transfers through device. Each photograph is time exposure of about 200 traces, with noise level near 10-rms electrons.

$N_{mes} \approx 300,000\ e^-$

100 e^-

20 e^-

Fig. IV-2. Examples of imaging test in which device is illuminated with stroboscope having output duration much less than clock period of imaging array clocks. Device temperature is $-55°C$, and number of electrons indicated is average signal in bright areas of image.

In these measurements, the dark current contributed about 4 electrons to the output signal. When this device is used in a satellite surveillance system, the night-sky background would provide a background charge of about 30 electrons per pixel (depending on seeing conditions). This "slim zero" can be of use in improving the CTI of otherwise marginal devices.

The imaging capabilities of this device at low-light levels can be demonstrated by a novel technique. The CCD is designed to operate in a time-delay-and-integrate (TDI) mode, with continuous clocking of the imaging portion of the device. However, we can simulate conventional frame-imaging by using a stroboscope to illuminate the device. The stroboscope illumination lasts for only 10 to 20 μs compared with a vertical transport clock period of 1 ms, so the CCD can be clocked continuously while the stroboscope acts as a shutter for the resolution test-pattern image. The photographs in Fig. IV-2 show the results of this test at various illumination levels. The number of electrons indicated in the figure is the average number per pixel in the light areas of the image. The temperature of the device is approximately $-55°$C. Each photograph of the display monitor is the result of only one video scan from the device, so there is no temporal averaging effect from viewing multiple frames, as occurs in conventional TV displays. This is a particularly outstanding device because, with one faint exception near the left edge, there are no dark-current blemishes. Such blemishes would appear as bright vertical streaks in the display.

Another feature is the two faint vertical dark lines in the two lower photographs of Fig. IV-2: one to the lower right of the horizontal pattern of the largest element "3," and the other near the upper-right-hand corner of the vertical pattern of the largest element "4." Using imaging tests and transfer inefficiency measurements, we have determined that these features are a trapping mechanism in isolated CCD wells. These charge traps hold a fixed amount of charge, which in other devices varies from less than 100 to about 5000 e⁻, and emit the charge over time periods as long as 1 s at $-50°$C. This appears to be the first observation of this type of defect, and further studies will be needed to determine its origin. Fortunately these defects occur in small numbers, usually no more than five per chip, and are the only significant charge loss mechanism in these CCDs.

B. E. Burke

B. CHARGE-COUPLED DEVICES: LATERAL H₂ DIFFUSION TO REDUCE SURFACE STATES IN DUAL-DIELECTRIC STRUCTURES

This report describes a hydrogen-ambient annealing procedure for dual-dielectric (SiO_2-Si_3N_4) insulated gate structures. Hydrogen anneals have proven essential for the neutralization of both surface states at the silicon-silicon oxide interface and bulk point defects near this silicon surface.[3] Unfortunately, the presence of Si_3N_4 over the SiO_2 gate dielectric acts as a H_2 diffusion barrier at process temperatures compatible with aluminum metallization ($<500°$C). We have observed, however, that long-term annealing in H_2 permits lateral diffusion in the SiO_2 layer from the edges of the scribe apart groove around each chip. By using an imaging CCD, the progress of the anneal can be measured on a video display.

The variant of the LOCOS[4] process we use to fabricate n-MOS and CCD devices has been described previously.[5] Our process utilizes 800 Å of thermal SiO_2 capped by 600 Å of chemically vapor-deposited Si_3N_4 to form the gate dielectric. Because Si_3N_4 acts as a diffusion barrier to H_2 at temperatures compatible with aluminum metallization,[6] the final fast interface state anneal must occur by diffusion initiated at openings in the Si_3N_4 and proceeding laterally through

39

the SiO_2 under the Si_3N_4 layer. Unless there are pinholes in the Si_3N_4, the H_2 must diffuse a long way in a CCD imaging array where no vias or contact windows exist.[7]

For the experiment performed in our laboratory, the GEODSS CCD imager[2] was used. This chip is 13.3×3.6 mm, and is fabricated by a process in which Si_3N_4 is deposited on both the dual-dielectric gate and ~6000-Å-thick field-oxide regions. As a result, H_2 diffusion is initiated only from the chip periphery where scribe lines around the chip open the Si_3N_4. Although there are contact windows through the Si_3N_4 for clock lines and input and output FETs, H_2 diffusion at these sites is completely blocked by the aluminum metallization.

The effect of conventional H_2 annealing for reduction of surface states saturates in the absence of Si_3N_4 at about 20 to 30 min. at 400°C. When Si_3N_4 is present, even 1-h periods are inadequate. Figure IV-3(a) is a photograph of the video output of an unilluminated imaging CCD after a 1-h H_2 anneal at 400°C. The light central region results from dark current on the order of 100 nA/cm^2, corresponding to high levels of unannealed surface states. The dark regions around the periphery of the chip indicate the extent to which H_2 diffusion has neutralized surface states and possibly buried channel point defects. In these regions, the dark current is on
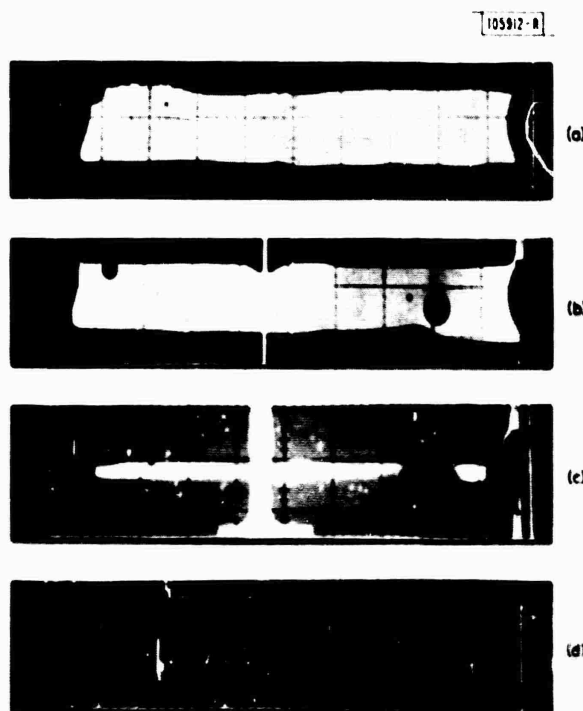
Fig. IV-3. Video displays of four GEODSS CCD imagers with no illumination. Light areas in center of device are result of video signal due to dark current which results from high density of surface states at active Si-SiO$_2$ interface. These photographs show neutralization of defects and surface states after annealing at various times at 400°C. H_2 must diffuse into SiO$_2$ from periphery of imaging chip as device is completely capped by Si$_3$N$_4$. Black "holes" indicate pinholes in nitride layer through which local diffusion of H_2 into SiO$_2$ can take place. Vertical white stripes and isolated white spots result from channel leakage defects which are unrelated to these annealing experiments. (a) and (b) 1-h. (c) 9-h. and (d) 15-h anneal.

the order of 1 to 2 nA/cm^2. The light spots and vertical lines in all the photographs are channel leakage defects unrelated to surface state defects, and correspond to dark currents of about 10 nA/cm^2. Figure IV-3(b) is the same video display, but for a different chip. Here dark "holes" appear in the high dark-current region. These holes are the result of local H_2 annealing through nitride pinholes. These nitride pinholes do not necessarily result in device failures, since the fabrication sequence calls for a special oxidation step to fill in these Si_3N_4 defects. Figure IV-3(c) is the video display of another GEODSS chip after 9 h of H_2 anneal (400°C). In this instance, the anneal appears close to completion, although it is clear that H_2 diffusion is nonlinear with time. Another device of the same lot after 15 h of H_2 anneal is shown in Fig. IV-3(d). No evidence of dark current due to surface states is evident even when a higher electronic gain is used in the video detection circuit, although some channel defects are readily apparent.

Brown et al.[8] have measured the diffusion of H_2 through thermally grown 700-Å SiO_2 films on Si capped by 400-Å Si_3N_4, and found that the diffusion from the exposed SiO_2 proceeds at a rate proportional to the square root of the anneal time. Figure IV-4 is the curve of the rate of
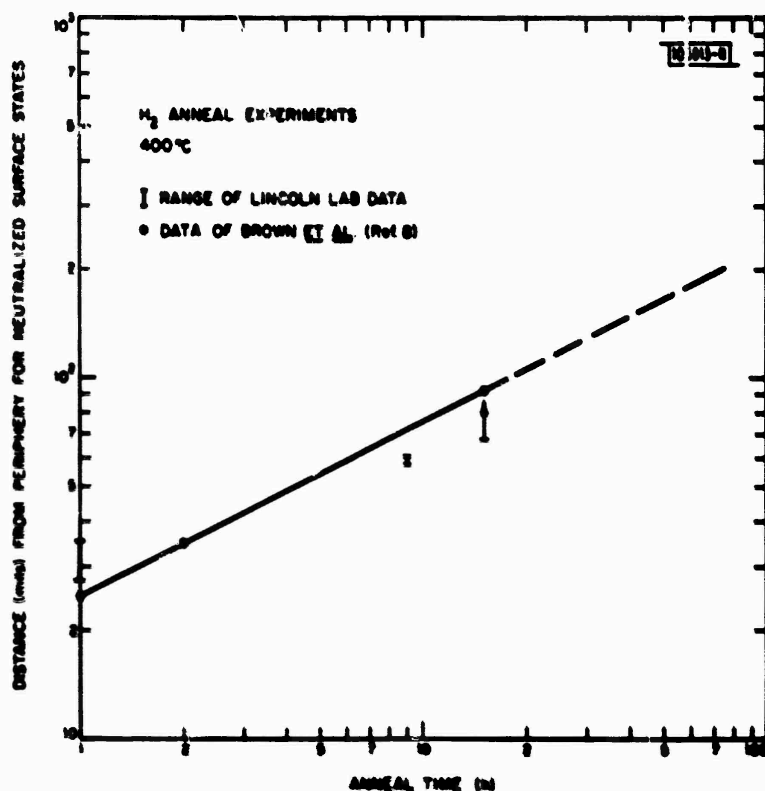
Fig. IV-4. Data of Brown et al.[8] predicting motion of low-high dark-current interface from imaging chip periphery as function of time. Brackets indicate range of data for experiment described in text. Bracket at 15 h has undetermined maximum as defects on devices were completely annealed out after this period.
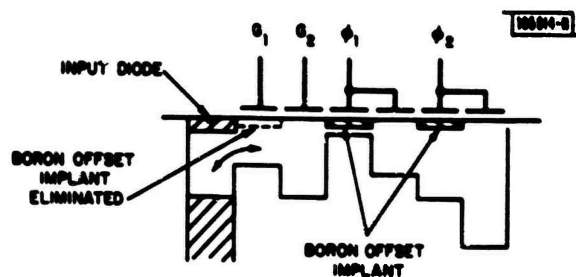
Fig. IV-5. A "fill-and-spill" CCD input showing elimination of offset implant under G_1 gate.
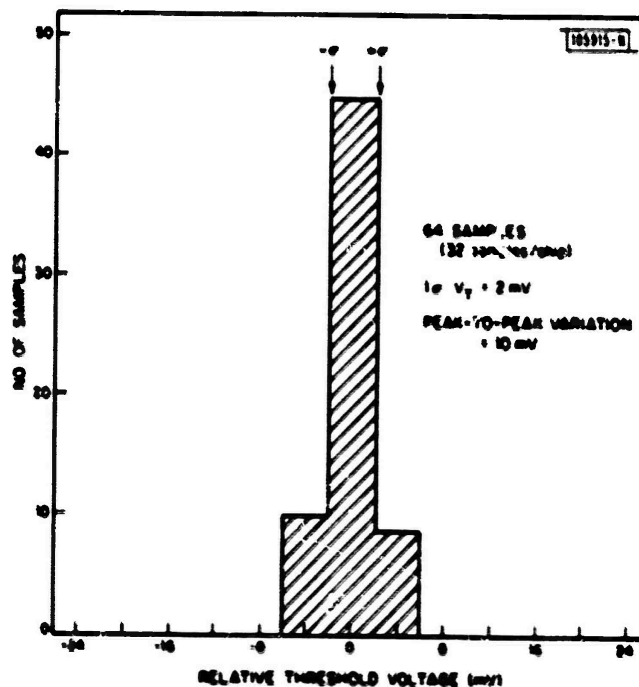
Fig. IV-6. Histogram for threshold-voltage variation of surface-channel input structure with boron implant under G_1 gate eliminated. Devices are fabricated on 25- to 45-Ω-cm Czochralski starting material.

motion of the H_2 fast surface state annealing replotted from the data of Brown et al. Superimposed on this work is the bracketed range of our data points. Our results are qualitatively in agreement.

D. J. Silversmith
B. E. Burke
R. W. Mountain

C. CHARGE-COUPLED DEVICES: PROGRAMMABLE TRANSVERSAL FILTER

As previously reported, the effect of both input-gate capacitance variation[9] and threshold-voltage variation (see Ref. 2, pp. 61-65) on the performance of our high-speed CCD programmable-transversal-filter (PTF) structures is to allow different amounts of signal charge to enter the parallel delay lines for the same signal voltage applied to the input gates. This phenomenon limits the dynamic range and bit accuracy of multi-level tapweight filters. Our present CCD fabrication process has reduced the relative input-gate capacitance variation to a 1-σ value of less than 1 percent among 32 parallel inputs on a typical PTF device. The threshold-voltage variation resulting from inhomogeneity in substrate doping and implant dosage has been modeled, and a 1-σ variation of 5 mV was obtained by using surface-channel inputs (Ref. 2, pp. 61-65). The model also predicted that a surface-channel input device with the boron offset-implant under the input gate eliminated would further reduce the threshold nonuniformity. Recent test results agree with the model calculation and are reported here. A 1-σ threshold variation of 2 mV and a peak-to-peak variation of 10 mV among 32 channels has been achieved consistently on our PTF devices.

A commonly used "fill-and-spill" input structure is shown in Fig. IV-5. The input or signal voltage is applied to either the G_1 or G_2 gate, while the other gate is held at a reference voltage. The threshold voltage of the device is the signal voltage which will cause the channel potential under the two gates to be equal. When a CCD filter consists of parallel input channels with common signal and reference gates, the threshold variation of the device is the difference in signal voltages at which potential equilibration takes place for each channel.

As reported previously (Ref. 2, pp. 61-65), the threshold variation depends on the input structure and the doping profiles under the two gates. However, the two-phase CCD process[10] used for our early PTF devices resulted in a boron offset-implant under the G_1 gate. Based on our calculations, a 1-percent variation in this boron-implant dosage would lead to a 20-mV threshold variation, which is in agreement with our experimental results. Our model also showed, however, that if high-resistivity starting material ($\rho > 15$ Ω-cm) is used and the boron implant in the gate region is eliminated, a 1-percent variation in the starting-material doping should result in a threshold variation of less than 10 mV.

To test the model, three different types of starting material were used to fabricate PTF devices using a new process that eliminates the boron implant under the G_1 gate. The materials were 25- to 45-Ω-cm Czochralski material, 30- to 50-Ω-cm float-zone material, and 100- to 150-Ω-cm float-zone material. PTF devices with 32 parallel channels were used, and extensive measurements were taken on devices of each starting material. A typical 64-sample (32 samples/chip) histogram from the Czochralski starting material (Fig. IV-6) shows that a 1-σ variation of 2 mV and a peak-to-peak variation of 10 mV have been achieved. This result suggests that local fluctuation in substrate concentration of Czochralski material is about 2 percent. Test results obtained from float-zone starting material showed a much higher degree of local fluctuation. The 100- to 150-Ω-cm float-zone starting material had a 1-σ variation of 5.7 mV and a peak-to-peak variation of 20 mV.

The techniques used to measure the threshold voltage are of interest. The linear region of output- vs input-signal voltage for each CCD channel is measured first. A linear least-square (LSQ) fitting of test data is then used to determine the input voltage which gives zero output for each channel. This input-signal voltage is then defined as the threshold voltage of the channel. The threshold voltage determined by this method is independent of the input-gate area and should be more accurate than that determined by the commonly used constant-current or constant-voltage methods.[11] Another advantage of using this measuring technique is that the input-gate capacitance of each channel can be derived from the slope of the LSQ curve.

In conclusion, there are two process parameters affecting the performance of our high-speed CCD filter, i.e., capacitance variations and threshold variations among the parallel input gates. Our wafer processing results in good capacitance uniformity (1 σ less than 1 percent) and, using higher-resistivity Czochralski starting material without a boron offset-implant in the input regions, we obtained a 1-σ threshold variation of less than 2 mV for our recent PTF devices.

A.M. Chiang   D.J. Silversmith
B.E. Burke   R.W. Mountain

D. MILLIMETER-WAVE MONOLITHIC GaAs RECEIVER

A 2.5- × 5-mm receiver circuit has been fabricated on a semi-insulating GaAs substrate. The receiver chip is comprised of a 31-GHz double-balanced mixer and a 2-GHz IF amplifier (see Ref. 2, p. 65). This prototype was developed as part of a program seeking to establish the feasibility of GaAs monolithic receivers and transmitters at millimeter-wave frequencies. High-performance planar Schottky diodes in the mixer circuit with cutoff frequencies above 100 GHz provide the capability of extending this approach to frequencies beyond the operating range of receiver designs using FETs only. However, monolithic receiver designs using Schottky-barrier mixer diodes require the development of a fabrication process integrating microwave diodes and FETs. Because high-cutoff-frequency diodes require an n-on-n$^+$ active layer for low series resistance and MESFETs require only an n-type layer, different epitaxial requirements are imposed on the same semi-insulating GaAs wafer. The development of a compatible integration scheme is fundamental in establishing the feasibility of this approach for monolithic receivers at millimeter-wave frequencies.

The photograph in Fig. IV-7 shows the monolithic receiver chip, which measures 2.5 × 5 mm. The balanced mixer is located in the upper portion of the chip above the FET IF amplifier. The mixer diodes have a junction area of 30 μm^2. The zero-bias junction capacitance is typically 0.06 pF, and the series resistance is 12 Ω. The mixer diodes are connected to the output arms of a 90° branch-line coupler which combines the signal and local-oscillator (LO) signals. Balanced mixers with minimum conversion losses of 5.5 dB for a signal frequency of 31 GHz and an IF of 2.26 GHz have been fabricated. Typical conversion-loss results are 6 dB. The input matching network of the IF amplifier consists of a pair of open-circuited stubs cascaded with a 140-Ω transmission line. Typical parameters of the 1- × 500-μm-gate MESFET are: drain saturation current of 100 mA, transconductance of 50 mmhos, and pinch-off voltage of 2.5 V. No output matching circuit was fabricated on this chip since it will ultimately be combined with the input matching circuit of a second-stage amplifier to form an interstage matching network. Amplifier noise figures of 2.4 dB have been measured at 2 GHz, and typical performance for this single-stage amplifier is 3 dB. Multistage amplifiers of two and three stages using this amplifier chip have 20 and 30 dB gain, respectively, and a noise figure of 3.5 dB over 1-GHz bandwidth centered at 2.3 GHz.

Fig. IV-7. Monolithic GaAs receiver
chip showing 31-GHz double-balanced
mixer (top) and 2-GHz IF amplifier
(bottom).
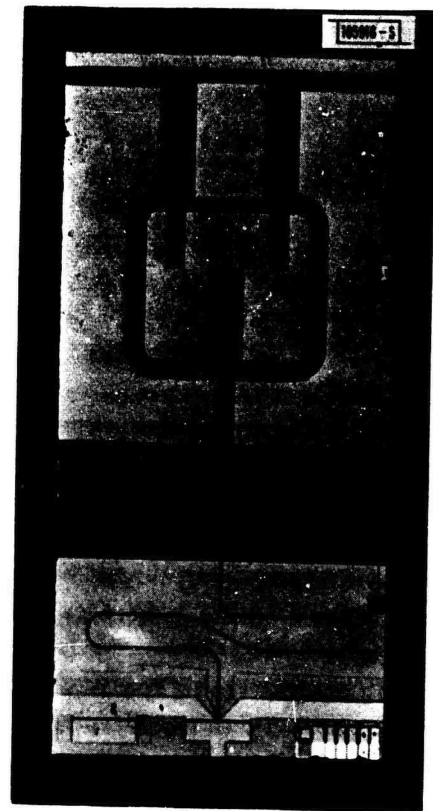
The RF performance of the initial monolithic receiver prototype is illustrated in Fig. IV-8
in which SSB receiver noise figure and overall gain are shown as a function of the intermediate
frequency (IF). In this measurement, the LO was at 29 GHz and the signal frequency was
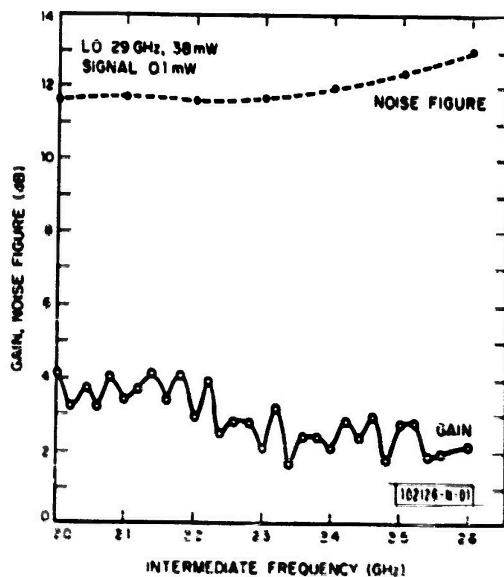
Fig. IV-8. Performance of initial
monolithic GaAs receiver for sig-
nal frequency varied between 31.0
and 31.6 GHz.

104787-N-01

COVER

50-Ω MICROSTRIP

MIXER RF

LO IF

FIXTURE'S MAIN BODY

COAXIAL PROBE

COAXIAL PROBE

WAVEGUIDE COUPLER

COAXIAL CONNECTOR

TUNING SCREWS

WAVEGUIDE COUPLER

RF WAVEGUIDE SECTION

TUNING SCREWS

LO WAVEGUIDE SECTION
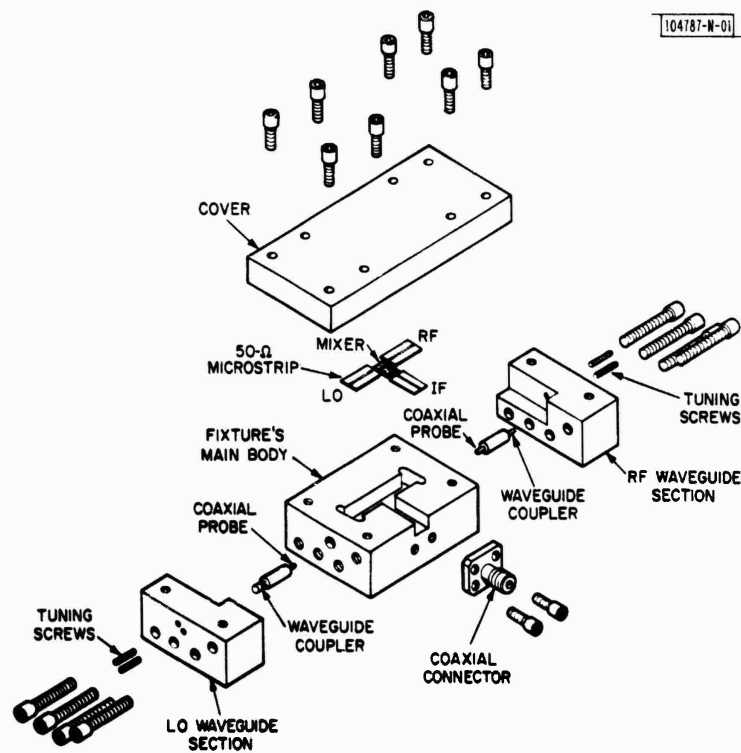
Fig. IV-9. Exploded view of K_a-band test structure.

ION IMPLANTER

103727-N-01

150-keV H$^+$ BEAM

MEMBRANE (1 μm)

ABSORBER

PMMA-COATED WAFER

ENERGY LOSS: ~100 keV/μm (polymer)

DOSE: $2 \times 10^{13}/cm^2$

Fig. IV-10. Schematic diagram of ion-beam exposure process.

varied between 31.0 and 31.6 GHz. Between 2.0 and 2.3 GHz, the conversion gain and noise figure are approximately 4 and 11.5 dB, respectively.

Measurements and noise-circle analysis of multistage IF amplifiers indicate that an improved low noise match will yield receivers with a noise figure lower than 10 dB. With two amplifier stages the receiver chip will have a conversion gain of 14 dB, which is adequate for many systems applications.

The K_a-band test fixture used to test the receiver circuit has a 25-percent bandwidth and an insertion loss of less than 1 dB for each input to the balanced mixer. An exploded view of the fixture (Fig. IV-9) shows the main body of the test fixture together with the units which constitute the waveguides for the LO and RF signals. A set of tuning screws provides RF tuning for each waveguide for minimum insertion loss. The LO and RF signals are coupled by coaxial probes through the broad wall of the main body of the fixture directly to microstrip on the alumina substrate. The fixture is split to facilitate the insertion of the waveguide coaxial probe units and the thermocompression bonding of the module. To avoid pressure contacts on the brittle input and output sections of the GaAs, 50-Ω alumina microstrip transmission lines are located between the coaxial probe section and the module. This enable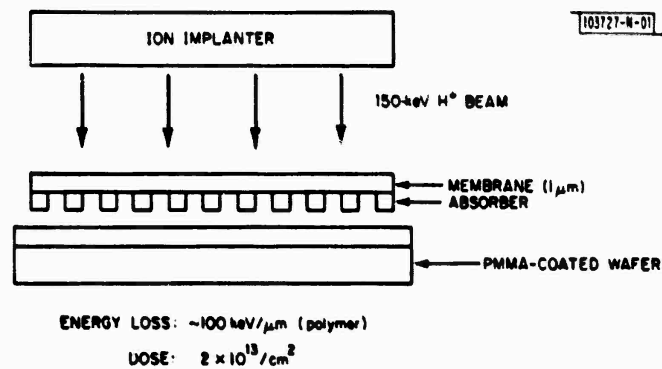s the input and output sections of the GaAs module to be connected with an appropriate thermocompression-bonded ribbon. The IF output is provided by a coaxial connector which contacts the microstrip directly. The waveguides are formed by attaching the cover.

This fixture is compact and easily tuned, and provides direct coupling from waveguide to microstrip. It can accommodate a wide variety of modules for testing, and can be easily expanded for multistage amplifier systems.

A. Chu   W. Macropoulos
W. E. Courtney (Grp. 33)   G. A. Lincoln
L. J. Mahoney

E. ION-BEAM LITHOGRAPHY

Ion-beam exposure of resists is a promising new lithographic technique for the reproduction of patterns having submicrometer features.[12] Both high resolution (~200 Å) and short exposure times (<1 s) should be possible. The main difficulty is the development of a suitable mask technology which will provide sufficient contrast with a minimum of scattering of the incident beam. In this report, we describe initial resist exposure experiments using a new type of ion-beam mask.

The exposure process is shown schematically in Fig. IV-10. A conventional ion-implantation system is used to generate a beam of protons whose energy can be varied from 50 to 400 keV. The roughly collimated beam is incident on a mask consisting of an absorber pattern on a thin support membrane. The mask is held in intimate contact with a PMMA-coated substrate. Beam energy is selected so that the protons pass through the support membrane and emerge with sufficient energy to expose the resist, but are stopped by the combination of the membrane and absorber. The pattern is thus transferred to the PMMA.

The mask developed for these experiments is shown in Fig. IV-11. It consists of a single, freestanding polyimide membrane[13] approximately 2 μm thick. A grating pattern having 1.2-μm lines on 3.8-μm centers was etched into the membrane to a depth of 1 μm by oxygen reactive-ion etching.[14] Contrast for the proton exposure of resist was provided by the modulation in membrane thickness, the polyimide acting as both absorber and support membrane. The stopping

47

[103729-N-01]

$2\,\mu m$ $1\,\mu m$

ABSORBER — 2-μm POLYIMIDE
MEMBRANE — 1-μm POLYIMIDE
FABRICATION — OXYGEN RIE
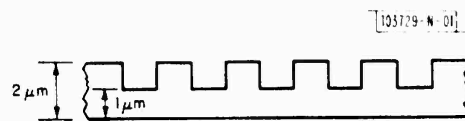
Fig. IV-11. Ion-beam mask using polyimide as both absorber and support membrane.

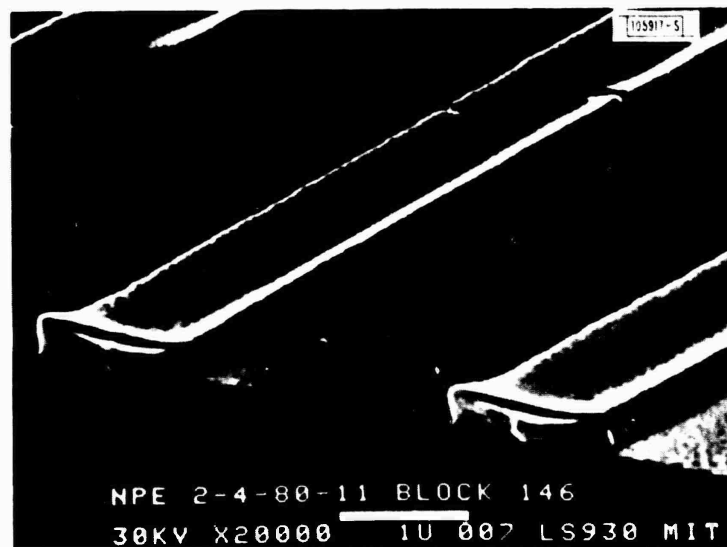NPE 2-4-80-11 BLOCK 146
30KV X20000 1U 007 LS930 MIT

Fig. IV-12. Scanning electron micrograph of proton-exposed grating pattern in PMMA.

power of polyimide was determined by measuring the transmission of protons through membranes of known thickness as a function of incident beam energy. In the energy range from 50 to 300 keV, the stopping power of polyimide for protons was found to be ~100 keV/μm, independent of energy. The stopping power of PMMA for protons in this energy range is also ~100 keV/μm (see Ref. 15). Therefore, a beam energy of 150 to 200 keV was required to expose a 0.5-μm thickness of PMMA through the mask. For a dose of 2×10^{13} protons/cm^2, complete development of the exposed areas was obtained in 1 min. using a 60-percent isopropyl alcohol, 40-percent methyl isobutyl ketone solution.

Figure IV-12 is a scanning electron micrograph of proton-exposed PMMA. This sample was exposed at an incident beam energy of 175 keV. As can be seen, the mask pattern has been faithfully reproduced in the resist. The vertical sidewalls of the PMMA lines show that the potential resolution is much better than the 1.2-μm linewidth shown here. Part of this sample was coated with 200 Å of Cr and a successful lift-off was performed, again indicating the steepness of the sidewalls.

In conclusion, we have successfully developed a new all-polyimide mask for proton exposure of resists. Resolution of 1.2 μm has been demonstrated, and there is clear indication that much better resolution is possible.

<div align="right">

N. P. Economou
D. C. Flanders
J. P. Donnelly

</div>

F. SILICON GRAPHOEPITAXY

In earlier papers,[16-18] we described experiments on graphoepitaxy[†] of silicon films over amorphous fused silica substrates in which a scanning CW argon-ion laser was used to induce crystallization of the silicon film, and a surface-relief grating having a square-wave cross section was used to induce orientation. Here, we discuss an alternative approach in which the laser is replaced with a strip-heater oven, and we compare the crystallographic and the electrical properties of graphoepitaxial silicon films produced by the laser and oven techniques.

The strip-heater oven, shown schematically in Fig. IV-13, consists of two 50- × 75- × 1.2-mm resistively heated carbon strips. The sample, which is placed on the lower strip heater, consists of a substrate with a deposited film of silicon and a deposited film (or "cap") of SiO$_2$; the SiO$_2$ cap was necessary to achieve graphoepitaxy. The substrate is either fused silica, as in earlier work,[16-18] or thermally grown SiO$_2$ (usually ~1 μm thick) on a silicon wafer. A relief grating of square-wave cross section and grating period ranging from 1 to 4 μm is etched 100 nm deep into the SiO$_2$. The grating periods used to date are in the 1- to 4-μm range. The sample is heated on the lower strip to 1100° to 1300°C, after which additional radiational heating by the upper strip causes crystallization to occur in the silicon. After this transition, the mean $\langle 100 \rangle$ crystallographic directions are perpendicular to the substrate and parallel to the grating axis. The entire crystallization process requires about 40 to 60 s. A more detailed description of the process is published elsewhere.[19]

The graphoepitaxial silicon films produced either by strip-heater oven or laser crystallization are mosaics, with crystallites having a range of orientations relative to the substrate normal and the grating axis. Each crystallite can be characterized by two angles: Θ, which is

---

[†] Graphoepitaxy is a new term coined to designate processes in which an artificial pattern on a surface is used to control orientation in a film.

100162-N-03

UPPER STRIP HEATER

LOWER STRIP HEATER

SAMPLE

CROSS SECTION

SiO$_2$

Si

SiO$_2$
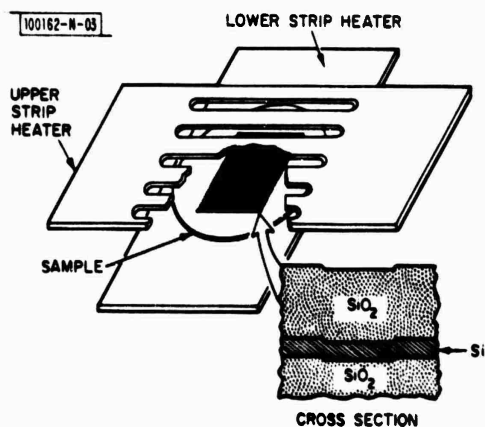
Fig. IV-13. Schematic diagram of strip-heater oven used for silicon graphoepitaxy. Inset shows cross section through sample. Slits in upper strip permit visual observation of crystallization process.

Fig. IV-14. Illustration of effect of patterning on texture of crystallized silicon films. In all cases, silicon is deposited on smooth SiO$_2$ surface, capped with 2 μm of SiO$_2$, and crystallized in strip-heater oven. (a) Illustrates that (100) texture is obtained for case of continuous silicon film, (b) that (111) texture is obtained if silicon is patterned into stripes 3 to 25 μm wide and several millimeters long, and (c) that weak (110) texture is obtained if silicon is patterned into rectangles 3 to 25 μm on a side.

105910-R

(100) TEXTURE

(a)

(111) TEXTURE

(b)

WEAK (110) TEXTURE

(c)
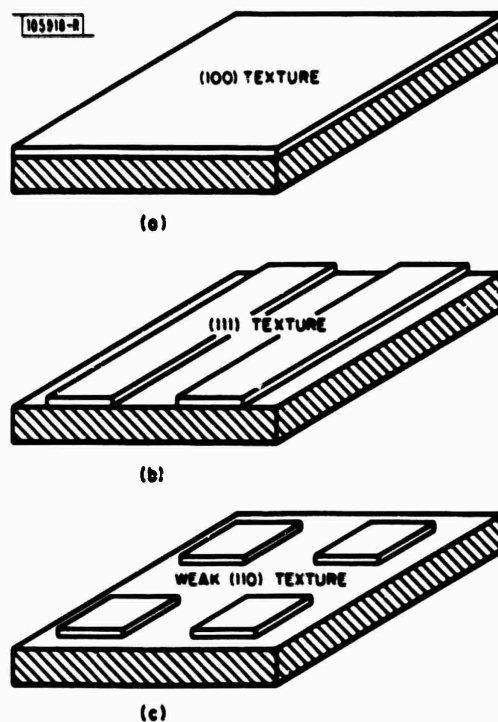
the deviation of the $\langle 100 \rangle$ direction from the substrate normal; and ϕ, which is the deviation of the $\langle 100 \rangle$ direction from the grating axis. For a large-area film, the values of Θ and ϕ have a distribution about some mean value. The half-width at half-maximum (HWHM) of the Θ distribution is called the "tip angle," and the HWHM of the ϕ distribution is called the "spread angle." For laser crystallized films the best tip angle obtained was 1.5°, while the tip angle for strip-heater crystallized films ranged from 0.25° to 0.75°. The best spread angle obtained in laser crystallized films was 8°, while the spread angle ranged from 3° to 7° for oven crystallized films. Silicon films crystallized with the strip-heater oven are free of the short-period surface roughness that characterizes laser crystallized films.[16-19] Microcracks, which apparently arise from differential thermal expansion, do not occur if the substrate is thermally grown SiO_2 on a silicon wafer.

The graphoepitaxial silicon films have been electrically characterized by fabricating enhancement mode, n-channel, insulated polysilicon-gate field-effect transistors. The transistors fabricated in oven crystallized silicon had electron surface mobilities that ranged from 300 to 460 cm^2/V-s. Similar devices could not be fabricated in laser crystallized films due to surface roughness and microcracks. However, electron Hall mobilities of the laser crystallized films could be measured, and ranged from 325 to 980 cm^2/V-s at doping levels of 5 to 8×10^{16} cm^{-3}.

Graphoepitaxy of silicon, whether by laser or oven crystallization, has been achieved only when a cap of SiO_2 covers the silicon film. If such a cap is absent or the silicon is fully melted, a polycrystalline film is obtained that exhibits neither texture nor orientation relative to a surface relief grating. The mechanism through which the SiO_2 cap induces texture and orientation is not understood. It is interesting to note that the texture is dependent on the shape of the silicon film when it is crystallized. If a continuous silicon film on a smooth substrate is capped with 2 μm of SiO_2 and crystallized in a strip-heater oven, a (100) texture is obtained — as illustrated in Fig. IV-14(a-c). However, if the silicon film is patterned into stripes 3 to 25 μm wide and several millimeters long, capped with SiO_2 and oven crystallized, a strong (111) texture is obtained. If the silicon film is patterned into squares or rectangles 3 to 25 μm on a side, capped with SiO_2 and oven crystallized, only a weak (110) texture is obtained.

M. W. Geis
D. J. Silversmith
R. W. Mountain

REFERENCES

1. Solid State Research Report, Lincoln Laboratory, M.I.T. (1978:4), pp. 38-41, DDC AD-A068563/6.

2. Ibid. (1979:4), pp. 56-59, DDC AD-A084271/6.

3. J. L. Benton et al., in Laser and Electron Beam Processing of Materials, C. W. White and P. S. Percy, Eds. (Academic Press, New York, 1980), p. 430.

4. E. Kooi et al., Philips Res. Rep. 26, 166 (1971).

5. Solid State Research Report, Lincoln Laboratory, M.I.T. (1978:2), p. 40, DDC AD-A061241/6.

6. D. M. Brown et al., J. Electrochem. Soc. 115, 313 (1968).

7. R. C. Dockertz et al., Extended Abstracts, Electrochemical Society Mtg., Spring 1974 (74-1), Abstract 51.

8. D. W. Brown et al., IEEE J. Solid State Circuits SC-13, 5 (1978).

9. B. E. Burke and W. T. Lindley, Electron. Lett. 13, 521 (1977), DDC AD-A054405/6.

10. Solid State Research Report, Lincoln Laboratory, M.I.T. (1973:2), pp. 40-43, DDC AD-766233/1.

11. N. A. Foss, C. Garrison, and W. Larson, IRIS Meeting, Specialty Group on IR Detection and Imaging, Annapolis, Maryland, 13-15 June 1978.

12. M. Komuro, N. Atoda, and H. Kawakatsu, J. Electrochem. Soc.: Solid State Science and Technol. 126, 483 (1979).

13. D. C. Flanders and H. I. Smith, J. Vac. Sci. Technol. 15, 995 (1978), DDC AD-A061201/0.

14. P. D. DeGraff and D. C. Flanders, J. Vac. Sci. Technol. 16, 1906 (1979), DDC AD-A090069.

15. D. B. Rensch, G. Csanky, and H. L. Stover, Quarterly Report 2 for period 1 October – 31 December 1978, Hughes Research Corporate Research Laboratory (February 1979).

16. M. W. Geis, D. C. Flanders, and H. I. Smith, Appl. Phys. Lett. 35, 71 (1979), DDC AD-A076745/9.

17. M. W. Geis, D. C. Flanders, H. I. Smith, and D. A. Antoniadis, J. Vac. Sci. Technol. 16, 1640 (1979), DDC AD-A090072.

18. M. W. Geis, D. C. Flanders, D. A. Antoniadis, and H. I. Smith, IEEE International Electron Devices Meeting Technical Digest (IEEE, New York, 1980), p. 210.

19. M. W. Geis, D. A. Antoniadis, D. J. Silversmith, R. W. Mountain, and H. I. Smith, Appl. Phys. Lett. 37, 454 (1980).

V. ANALOG DEVICE TECHNOLOGY

A. TEMPERATURE-STABLE REFLECTIVE ARRAY COMPRESSOR (RAC)

Surface-acoustic-wave (SAW) dispersive delay lines in the RAC configuration have found many applications where large time-bandwidth (TB) products are required (see, for example, Williamson et al.[1]). The usual substrate for these devices is $LiNbO_3$, which has a temperature coefficient of delay (TCD) of $(1/\tau)(d\tau/dT) = 90$ ppm/°C in the z-direction of propagation and 70 ppm/°C in the perpendicular direction. A new cut of quartz[2,3] (RAC-cut quartz) has two orthogonal directions of SAW propagation with zero TCD, which makes possible the fabrication of temperature-stable RACs. The first such device is reported here. This RAC has a bandwidth of 50 MHz centered at 125 MHz and a dispersive delay of 38 μs, for a TB product of 1900. The performance is comparable to that of $LiNbO_3$, while the temperature stability is approximately 100 times greater.

To achieve a large TB product on RAC-cut quartz, two problems must be addressed: first, the small value of piezoelectric coupling limits the potential bandwidth available with conventional interdigital transducers (IDT); and second, the beam-steering angle of 3.4° must be compensated for in the design of the reflective grating. The device is shown schematically in Fig. V-1, and the properties of RAC-cut quartz are summarized in Table V-1.

The problem of transducer bandwidth has been solved by the use of edge-bonded transducers (EBTs). The theory and operation of EBTs on crystal-quartz SAW substrates have been described previously.[4] With EBTs, a fractional bandwidth of 40 percent is possible with low insertion loss, and center frequencies of 200 MHz are achievable. The device reported here uses EBTs with a center frequency of 125 MHz and approximately 4 dB insertion loss.

The RAC cut has a beam-steering angle of 3.4°, which means that the group velocity or power-flow direction differs from the direction of the phase velocity. Thus, the energy in an acoustic beam flows off at an angle of 3.4° relative to the launching direction, and would eventually miss a conventionally designed grating. Hence, the grating must be displaced to follow the power-flow direction while keeping the angle of the grooves at the value one would compute from the phase velocities, 45° for the case of RAC-cut quartz. However, we have shown[5] that the design of a pair of chirped reflective gratings consists of more than a simple displacement of the grating lines. In fact, the pair of gratings must be designed with different chirp slopes. We find that one reflection grating must have an increased chirp slope and the other must have a decreased value. The chirp slopes of the two arrays must satisfy

$$\Delta_1 = \Delta/(1 - \tan\theta)$$

and

$$\Delta_2 = \Delta/(1 + \tan\theta)$$

where θ is the beam-steering angle,

$$\Delta = \sqrt{2}\,\frac{d\pi}{5}\,\frac{2\Delta f}{\Delta T}$$

and $\Delta f/\Delta T$ is the desired chirp slope. This result does not consider beam steering in the transverse direction, as this beam steering can be compensated by a simple shift in the X-direction.
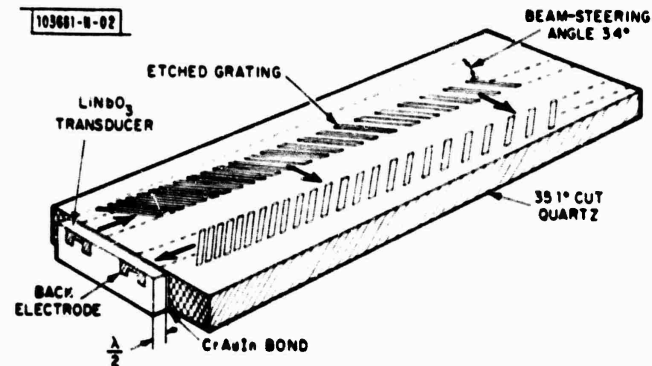
Fig. V-1. Temperature-stable quartz RAC.

TABLE V-1	
PROPERTIES OF RAC-CUT QUARTZ	
SAW Velocity	3267 m/s (both directions)
$\Delta v/v$	0.51×10^{-3}
Power-Flow Angle	3.4°
Cut Angle	35.1° rotated Y
Propagation Directions	± 45° from X
TCD $\frac{1}{\tau} \frac{d\tau}{dT}$	0 (both directions)
Reflection Grating Angle	45°

Since RACs with large TB products require long propagation distances, knowledge of diffraction losses is essential to the design of high-performance RACs. Because the velocity surface on this cut is nonparabolic, the usual approximations[6] for diffraction loss are not applicable. One must therefore calculate the SAW beam profiles using the general method of angular spectrum of plane waves developed for anisotropic media.[7] We have developed a new method for calculating diffraction profiles[5] which saves over a factor of 100 in computation time. Using this technique, we have calculated the expected diffraction loss on the RAC cut of quartz for a number of different aperture widths and crystal lengths. Table V-2 shows, for typical cases, the loss due to diffraction as measured at a receive transducer of the same width as the transmit transducer. This receive transducer is assumed offset by the 3.4° beam-steering angle in order to minimize loss. Results for propagation distances up to 2000 wavelengths have been verified experimentally. We can see from the table that for TB products greater than a few thousand, the diffraction loss on RAC-cut quartz is considerably greater than that on materials with a more nearly parabolic velocity surface, such as ST quartz.

TABLE V-2 DIFFRACTION LOSSES IN DECIBELS			
Transducer Aperture (wavelengths)	Propagation Distance (wavelengths)		
	1000	3000	6000
50	1.6	7.9	16.1
100	1.0	3.2	8.1
250	0.46	1.4	2.6

A RAC with a TB product of 1900 was designed according to the rules laid out above. The parameters of the device are given in Table V-3. The bandwidth was chosen to be one readily achievable with EBTs, and the dispersive delay is the maximum achievable with the available

TABLE V-3 RAC PARAMETERS	
Center Frequency	125 MHz
Bandwidth	50 MHz (downchirp)
Dispersive Delay	38 μs
Beam Aperture	77 λ
Substrate Length	7.62 cm
Grating Depth	2900 Å (unweighted)

RAC-cut substrate length. The grating was ion-beam etched to a uniform depth of 2900 Å. Depth weighting of the grating can be done in the standard fashion, but for reasons of simplicity a uniform etch was chosen. Figure V-2 shows device insertion loss, and Fig. V-3 shows the phase deviation from quadratic.
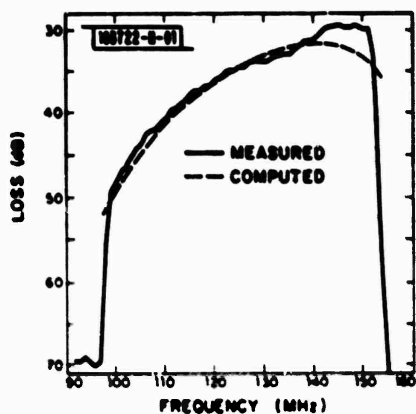

Fig. V-2. Measured and calculated insertion loss for temperature-stable RAC. Solid line is measurement. Broken line is computed curve normalized to measured value at 125 MHz. Calculation includes effects of reflection loss, diffraction loss, and propagation loss.
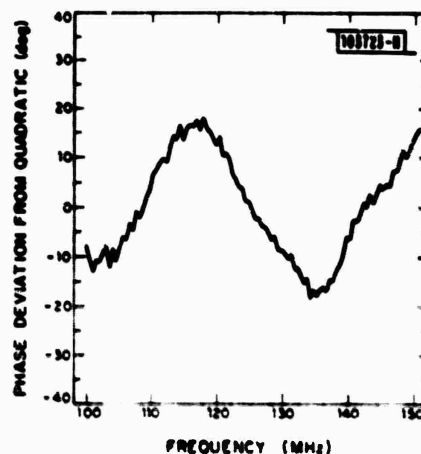
Fig. V-3. Measured phase deviation from expected quadratic phase dependence of temperature-stable RAC.

The shape of the insertion loss can be explained quantitatively with some simple considerations. The roll-off in the amplitude response at low frequencies is due in part to the uniform depth h of the ion-beam-etched grating. Since the reflectivity of a single groove at a wavelength λ is proportional to $h/\lambda \sim f$, and since the number of active grooves N_{eff} is also proportional to f, the reflectivity R of a pair of gratings is given by $R \sim [(h/\lambda) N_{eff}]^2 \sim f^4$. Thus, the grating reflectivity at 150 MHz is 7 dB greater than the reflectivity at 100 MHz. Since the device is a downchirp, diffraction and propagation losses further increase the total loss at 100 MHz relative to 150 MHz. The calculated diffraction loss at 100 MHz for parameters of this device is 5.5 dB. We estimate propagation loss at 100 MHz and 38 µs to be 3 dB. At 150 MHz, both diffraction and propagation losses are negligible. Computed grating reflectivity, diffraction loss, and propagation loss are shown by the dashed line in Fig. V-2. The agreement with the measurement is very good.

The phase vs frequency response is quite acceptable for a device without phase compensation. The phase deviation from quadratic is of order ±15°, which is a typical value for a device that has not gone through a phase-correction step. Measurements of the temperature dependence of the TB = 1900 quartz RAC are in progress. Preliminary measurements of temperature stability of narrowband devices showed stability about 100 times better than LiNbO₃ devices. As TB increases, the greater losses due to diffraction resulting from the longer propagation distances must be compensated by the depth of the grating. Although the amount of loss which can

be tolerated is somewhat application-dependent, about 10 dB of diffraction loss represents an upper limit that can be easily compensated by depth weighting. Calculations of diffraction loss for the RAC cut show that, at a TB product of 5000, the lowest frequency in a downchirp device experiences 10 dB of loss. Thus, a realistic limit of attainable TB product is approximately 5000 for temperature-stable RACs.

D. E. Oates
D. M. Boroson

B. ATTENUATING THIN FILMS FOR SAW DEVICES

A typical problem with SAW devices is the introduction of spurious signals in the response of these devices caused by reflections of the surface waves from the edges of the crystals. These unwanted signals are usually suppressed by using tape or grease placed on the surface of each crystal near the edges. In some applications, e.g., the use of these devices in satellites, these methods are inappropriate because they introduce contamination in the vacuum environment which degrades the performance of the SAW devices. In this report the use of thin films of cermets is described as an effective and vacuum-compatible way of suppressing edge reflections in SAW devices.

In a piezoelectric substrate, the propagation of a surface wave is associated with an RF electric field at the surface of the crystal. If a resistive film is deposited on the crystal, the electric field will induce currents in the film, dissipating energy so that the surface wave is attenuated.

A simple perturbation calculation[8] of the attenuation for a resistive film using an electrostatic approximation shows that, for an attenuation larger than 0.1 dB/wavelength (λ), the surface resistivity of the thin film has to be between 10^5 and 10^7 Ω/sq. Another important consideration is the thickness h of the film. If the film is too thick, mass loading will cause reflections at the boundary of the film. Since this effect is proportional in first order to h/λ, the thickness of the film should be limited to a small fraction of a wavelength.

The above considerations lead to requiring AC resistivity in the films of the order of 100 Ω-cm. Resistivities of this order can be easily obtained by the use of cermets.[9] By varying the amount of metal in the film, resistivities varying over several orders of magnitude can be obtained. Cermet films can be deposited by different methods, but sputtering is usually the method of choice. Both the Au/MgO and Cr/Cr_2O_3 cermet systems have been investigated with respect to stability, reproducibility of results, and adequate range of resistivity. The Cr/Cr_2O_3 system has produced the best results to date.

The films are deposited from a target of 30% Cr and 70% Cr_2O_3 in pure argon. For reproducibility of the results, it is essential that low base pressures be obtained prior to sputtering. The target is usually presputtered for at least 20 min. previous to the deposition of the films. The films are rugged, stable, and no special care in their handling is necessary.

Depending on their use, the films are deposited over the whole crystal and etched in ceric ammonium nitrate using conventional photolithography, or they can be sputtered through a metal mask. The second method is preferred when it is important to minimize reflections at the edges of the films, since the use of a shadow mask in a sputtering system produces a gradual edge that minimizes the effect of discontinuities at the boundaries of the films.

The SAW attenuation produced by each film was measured using a simple delay-line configuration. Strips of the cermet films were photolithographically patterned in the path of a delay line of known insertion loss. The additional insertion loss was then identified as the

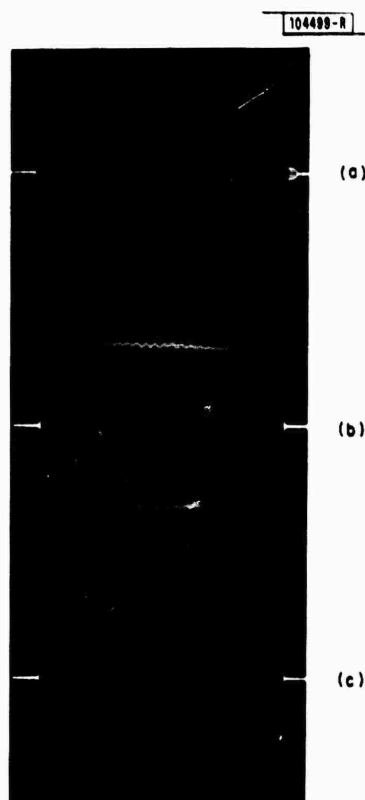| TABLE V-4 |||
| ATTENUATING FILMS (30% Cr and 70% Cr_2O_3) |||
Thickness (Å)	DC Resistance ($M\Omega$/sq)	Attenuation (300 MHz) (dB/λ)
600	6.45	0.09
850	4.5	0.22
1750	2.66	0.33

104489-R

Fig. V-4. Impulse response of RAC (a) with tape on output transducer, (b) with tape around four edges of crystal, and (c) with attenuating films behind both edges of crystal.

attenuation produced by the films. Additionally, the attenuation was determined by using a laser probe to measure the SAW intensity. The beam profile was determined in the region between the input transducer and the film, on the film, and on the output side of the film. The relative power levels were then obtained by integration of the area under the beam-profile curves. These methods produced essentially the same results. Films produced to date have attenuations between 0.06 and 0.4 dB/λ. Data for some typical films are shown in Table V-4.

Because the AC and DC resistivities for cermet films can be vastly different,[10] a direct comparison of RF and DC measurements is not appropriate. However, we have observed that for these Cr/Cr_2O_3 cermet films, the value of the DC conductivity can be used as a simple criterion for evaluating the attenuating properties of the films.

Our experience with wideband RACs indicates that reflection from a saw-cut edge will introduce a 1.6-dB amplitude ripple in the envelope of the impulse response. This reflection can be decreased by cutting the ends of the crystal at an angle different from 90° with respect to the propagation direction, but, unless the edges are polished and the other sides also angled, reflections can still occur. For reducing the ripple to 0.1 dB, an additional 24 dB of attenuation has to be introduced in the path of the interfering signal. This implies that if a film producing an attenuation of 0.4 dB/λ is used, it will have to be at least 30 λ wide.

In Fig. V-4(a-c) we compare the effectiveness of the suppression of spurious signals of an attenuating film 50 λ wide with that of polyimide tape. The two responses are indistinguishable. The residual spurious signals are due to bulk modes.

In summary, we have demonstrated that cermet films can be used as an effective, controllable, and vacuum-compatible method to attenuate surface waves. Their use to suppress reflections in SAW devices was demonstrated. Such films appear appropriate to trim the amplitude response of RACs as well.

A. C. Anderson   W. T. Brogan
V. S. Dolat   R. L. Slattery

C. HYBRID ANALOG/BINARY SIGNAL PROCESSOR

SAW convolvers[11] offer to the system engineer a method of implementing analog programmable matched filters with high bandwidths, while at the same time offering impressive processing gains. However, a dynamic range limitation is encountered when attempting to make very large time-bandwidth (TB) product convolvers, and this limits the processing gains achievable with convolvers to the 30-dB range.

There is a way to overcome the processing-gain limitation of SAW convolvers. By combining a convolver with binary-quantized postprocessing, it is possible to process waveforms with TB products of a million or more, thus providing in excess of 60 dB of processing gain. Such a processor could provide hundreds of time-offset correlations for very long, wideband waveforms. Recognizing that a convolver may be used as a matched filter for short waveforms, it is possible to construct the correlation of a long signal against a reference by using a convolver to provide the correlation of small pieces of the waveform and summing these in a second stage. The result can be a number of long-waveform correlations, each corresponding to a different time offset of the reference waveform. A very attractive means for the second-stage summation is binary integration. This combination of a convolver and binary circuits is shown schematically in Fig. V-5.

A binary integrator is a device which integrates a number of time-shifted replicas of an input waveform. In its simplest form, the binary integrator samples the input at precise intervals
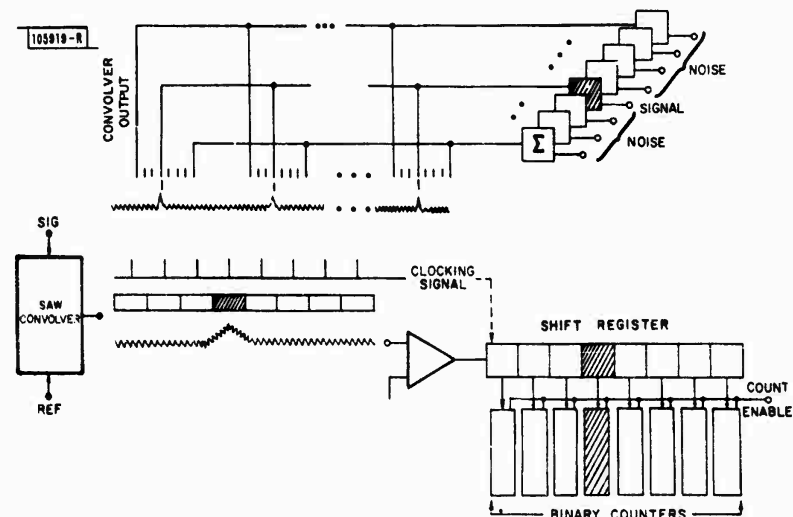
Fig. V-5.   Conceptual hybrid signal processor showing time window to deal with uncertain time-of-arrival.
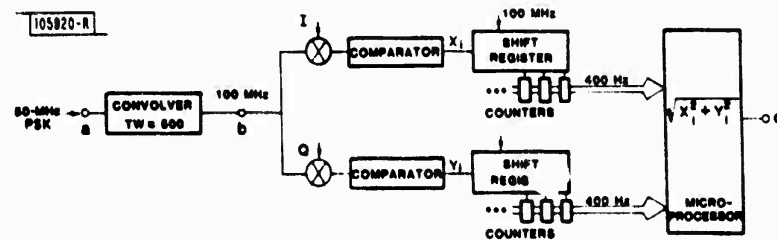

Fig. V-6.   Hybrid signal processing experiment.

and sums the result in a binary accumulator or counter. To implement this in hardware, the sampled signal plus noise is fed into a voltage comparator which converts the analog voltage to a binary level. With a strong signal present at the input, the comparator output will be 1 each time a sample is taken, and the counter will increment so that it contains a binary number corresponding to the number of samples taken. If we remove the signal so that only Gaussian noise (zero mean) is present, then the binary counter will increment one-half as many times, due to the statistical properties of Gaussian noise. With a weak signal present along with strong Gaussian noise, the number in the binary counter will be somewhere between the noise-only case and the strong-signal case, depending on the signal-to-noise ratio (SNR). Under the above conditions the integrator performs well, exhibiting only 2 dB degradation from ideal. The gain of the integrator is expressed as $3N-2$ (dB), where N is the number of binary stages. Thus, it becomes apparent that the gain of such an integrator is virtually unlimited, since more binary stages can simply be cascaded for additional gain.

However, if interference is present at the comparator input, and if the interference is, for example, of constant amplitude, then the comparator will be captured by the interference, and the circuit will not quantize the desired input signal properly. This problem has prevented the binary integrator from being widely accepted, although it is compact and simple both in concept and design.

By combining analog convolver preprocessing with binary integrator postprocessing it is possible to overcome the limitations encountered when using either technology alone. Thus, the binary integrator removes the convolver restriction on waveform time-duration and also overcomes the effect of limited convolver dynamic range. More importantly, the effect of the convolver processing gain is such that any interference presented to the convolver input has zero-mean and Gaussian-like statistics at the convolver output, which is presented to the comparator. Thus, the convolver acts to remove any potential vulnerabilities due to the use of binary integration.

The schematic of an experimental hybrid processor is shown in Fig. V-6. The main difference from Fig. V-5 is the inclusion of in-phase (I) and quadrature (Q) baseband detectors. I and Q detectors are required in order to achieve phase independence of the correlator outputs. Also note the eight parallel channels to resolve any time uncertainty of the convolver output pulse. The hybrid binary correlator uses a convolver with a TB product of 500 (27 dB) as the analog front end, and commercially available SSI and MSI components are used for the binary integrator. The shift register is an 8-bit serial-in/parallel-out device, and each binary counter is 8 bits long. Thus, maximum gain for this system is 27 dB (convolver) + 22 dB (binary integrator) = 49 dB, or a TB product of just under 100,000. The outputs of the binary counters are fed into a microprocessor, where the I and Q samples are used to form the magnitude of the correlation function. Of note is the effective bandwidth reduction from 100 MHz at the output of the SAW convolver to 100 kHz at the output of the shift register, and to 400 Hz at the output of the binary integrator. This property allows for the possibility of an extremely low-power, VLSI CMOS binary circuit.

To demonstrate the experimental hybrid correlator, a digitally encoded phase-shift-keyed (PSK) signal at the convolver input with a bandwidth of 50 MHz was varied in amplitude while a CW interference signal was applied at a fixed level of +16 dBm. The waveform in Fig. V-7(a-d) shows a small portion of the long PSK signal at -14 dBm (a), and a constant amplitude interference at +16 dBm (b) corresponding to an input SNR of -30 dB. The convolver output with no
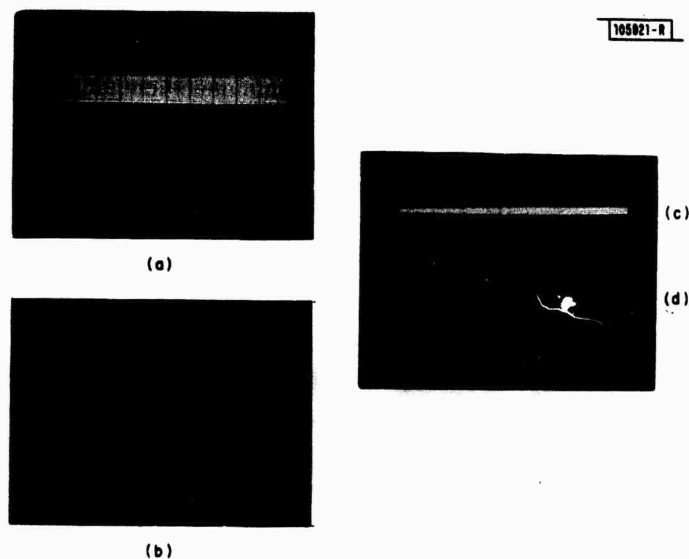
(a)

(b)

(c)

(d)

Fig. V-7. Test waveforms showing: (a) 50-MHz PSK waveform
(signal) at −14 dBm, (b) 300-MHz CW interference at +16 dBm,
(c) convolver output with no interference, and (d) convolver out-
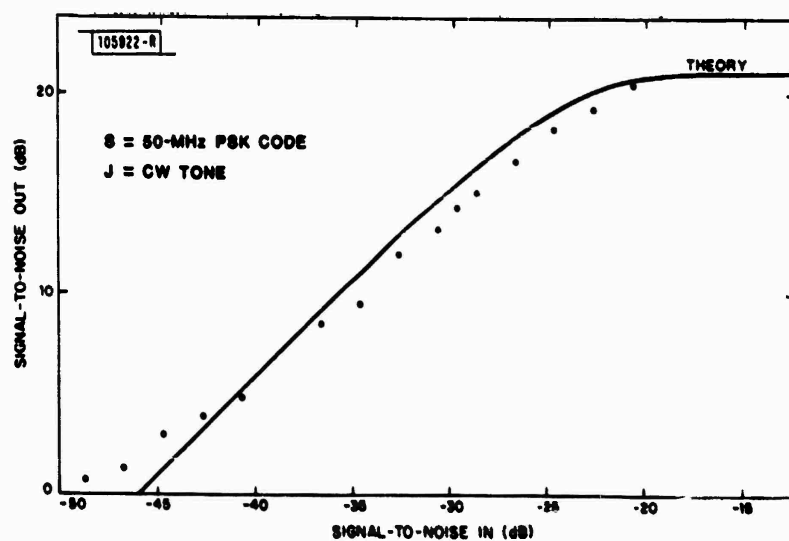put with interference.

Fig. V-8. Signal-to-noise out as a function of signal-to-noise in for theory
and experiment.

62